

# **Spirals and gravito-turbulence in 2D disks**

A dissertation submitted in partial fulfillment  
of the requirements for the degree of

**Master of Science (M.Sc.)**  
Astro and Particle Physics

28 September 2022

under the supervision of Prof. Dr. Klaus Werner  
& Dr. Christoph Schiesser

by

**Prakruti Sudarshan**  
Matrikel. No. 5731286

Eberhard Karls Universität Tübingen



## **Declaration of Originality**

This is to certify that to the best of my knowledge, the content of this thesis is an original report of my independent research. I have duly acknowledged all the sources from which the ideas and extracts have been taken. The project is free from plagiarism and has not been submitted elsewhere for any degree, publication or examination procedure. The copy submitted in file matches the bound copy.

Prakruti Sudarshan  
28 September 2022  
Tübingen



## Abstract

Modeling gravitational instabilities and the effects of turbulence in different scales provides insight into planet formation scenarios such as collisional growth and disk fragmentation. Gravitational instabilities can give rise to large-scale spiral arms in thin gaseous disks under slow, parametrized  $\beta$ -cooling in the absence of tidal forcing. With this project, we study gravitational turbulence in 2D using a prescribed cooling law. We characterize and explain the disk structure, and compare it to previous 3D analyses consisting of localized spirals. We examine the propagation of the flow and its correlation to viscous disk models. We perform 2D global numerical simulations of self-gravitating accretion disks using the GPU capable version of the finite-volume code PLUTO in two-dimensional cylindrical geometry with a self-gravity module. We vary disk mass and the cooling parameter  $\beta$ , and evolve our models sufficiently long to trigger the gravitational instability and the formation of spirals. Our models are significantly faster and computationally efficient compared to 3D global models of self-gravitating disks using grid and SPH methods. We find that the spirals show self-similarity and orient themselves into pitch angles that are constant in radius and time, close to those found in the 3D simulations. The values of turbulent stress  $\alpha$  from our models highlight the caveats of treating self-gravity in 2D. We also measure the radial and azimuthal wavenumbers of these spirals from their linear dispersion relation and check for fragmentation in cases of fast cooling.

# Contents

<b>1</b>	<b>Introduction</b>	<b>9</b>
<b>2</b>	<b>Disk physics</b>	<b>11</b>
2.1	Navier–Stokes equations . . . . .	11
2.2	The thin disk approximation . . . . .	11
2.3	Vertical disk structure . . . . .	12
2.4	The 2D equations . . . . .	12
2.5	Centrifugal balance . . . . .	13
2.6	$\beta$ cooling . . . . .	14
2.7	Dispersion relations . . . . .	14
2.8	Toomre criterion . . . . .	15
2.9	Stresses and angular momentum transport . . . . .	16
<b>3</b>	<b>Numerics</b>	<b>19</b>
3.1	Implementing self-gravity . . . . .	19
3.1.1	The 2D self-gravity approximation . . . . .	19
3.1.2	The GPU-CUDA self-gravity module . . . . .	20
3.2	Domain and integration scheme . . . . .	20
3.3	Initial and boundary conditions . . . . .	20
3.4	Units and model parameters . . . . .	21
3.5	On the indirect term . . . . .	22
3.6	Computing turbulent stresses . . . . .	22
<b>4</b>	<b>Tests</b>	<b>25</b>
4.1	Self-gravity: potential of a point mass . . . . .	25
4.2	Testing $\beta$ cooling . . . . .	26
4.3	A stable 1D disk . . . . .	26
<b>5</b>	<b>Results</b>	<b>29</b>
5.1	A reference simulation . . . . .	29
5.1.1	Illustration of the disk evolution . . . . .	29
5.1.2	Flow features . . . . .	30
5.1.3	The Toomre parameter . . . . .	31
5.1.4	On the disk aspect ratio . . . . .	32
5.1.5	Stresses . . . . .	33
5.1.6	Pitch angle of the spirals . . . . .	34
5.1.7	Dispersion relations . . . . .	35
5.2	Parameter survey . . . . .	36
5.2.1	Comparison of 2D surface densities . . . . .	36
5.2.2	High disk mass case: $q = 1$ . . . . .	37
5.2.3	Mass loss . . . . .	38
5.2.4	Toomre parameter and the disk aspect ratios . . . . .	38

5.2.5	Angular momentum transport . . . . .	39
5.2.6	Pitch angles and dispersion relations . . . . .	40
5.3	Comparison to the 3D simulations . . . . .	41
5.4	Resolution study . . . . .	42
5.5	A note about disk fragmentation . . . . .	44
<b>6</b>	<b>Discussion and conclusions</b>	<b>47</b>
<b>7</b>	<b>Acknowledgments</b>	<b>49</b>



# 1 Introduction

A lot of our theoretical understanding of planet formation comes from studying the structure, evolution and properties of protoplanetary disks (**PPDs**). Models include the widely accepted core accretion, which postulates the formation of a rocky core sufficiently massive to cause subsequent accretion of gas envelopes. There is an alternate theory, the gravitational instability (GI) model, which is based on the collapse of a massive protoplanetary disk under its gravity. A massive, cold gaseous disk can become gravitationally unstable and lead to fragmentation or settle into a system of stable angular momentum transport by generating spiral arms. The former is a formation mechanism for low-mass companions or giant planets (Cameron, 1978; Kuiper, 1951) and for star formation in disks around active galactic nuclei (AGNs, Nayakshin et al., 2007). The latter ensures redistribution of angular momentum that manifests into large-scale spiral arms (Lodato and Rice, 2004) when the disk cools over several orbital timescales. We consider gravitationally unstable disks with masses of a few fractions of the central object mass.

Several such disks exhibiting large-scale spiral structures which might be signatures of gravitational instabilities have been observed by ALMA and other partnerships (Mann et al., 2015; ALMA Partnership et al., 2015; Shepherd et al., 2001, 2004). Evidence of spiral arms could be seen in scattered light images of transition disks (Wagner et al., 2015; Muto et al., 2012) as shown in Fig. 1. The origin of these spirals have to be confirmed with mass constraints from ALMA data but could be attributed to self-gravity or the presence of a planet. However, the observed spirals have an  $m = 2$  symmetry and smaller pitch angles compared to what planet-induced spirals typically predict.

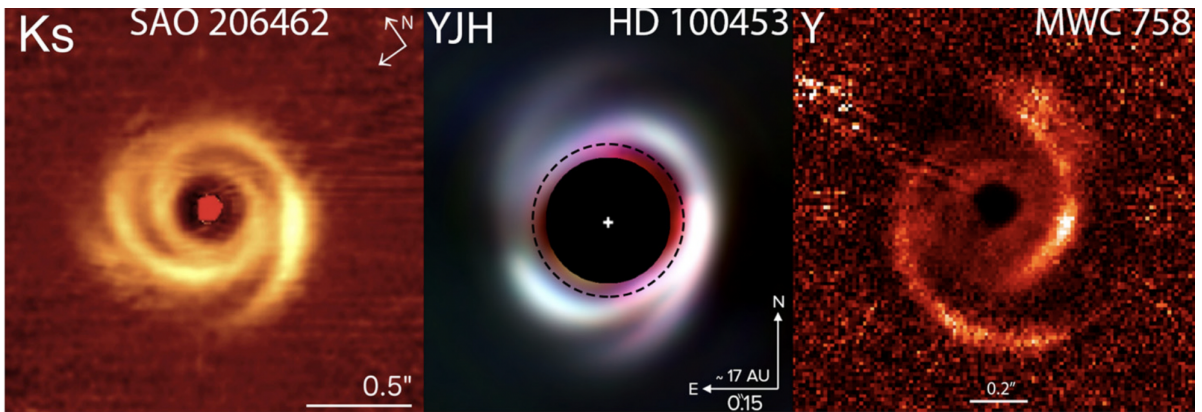


Figure 1. Three disks observed around young stars, with spiral features resolved in high-contrast imagery. Presented are disk images of SAO 206462 (Garufi et al., 2013), HD 100453, and MWC 758 (Benisty et al., 2015). The image is adapted from Wagner et al. (2015), who observed the HD 100453 system (VLT/SPHERE adaptive optics imaging).

Numerical simulations are key to understanding the physics of these gaseous and dust disk systems, due to the limited, wavelength-dependent information observations can provide. Local shearing-box simulations, that is, modeling sections of disks with local coordinates, are widely used to model self-gravitating disks in high spatial resolution (Gammie, 2001; Shi and

(Chiang, 2014; Young and Clarke, 2015) but these massive disks also produce wave modes that need to be captured globally. There have also been attempts to study such disks globally using SPH (Meru and Bate, 2011b,a; Lodato and Rice, 2004, 2005), grid codes in 2D and 3D (Boley et al., 2006; Steiman-Cameron et al., 2013), and around binary stars (Desai et al., 2019). Heating from the gravitational instability has various implications on the state of the disk based on the chosen cooling prescription (e.g., Gammie, 2001; Rice et al., 2005). Dominance of cooling results in disk fragmentation, but the disk can maintain a quasi-steady state for sufficiently short cooling timescales.

Cossins et al. (2009) performed Fourier analysis to characterize modes and pattern speeds associated with GI spiral structures from their SPH simulations and compared them with the linear theory of the WKB modes. They also quantified non-local processes from the dispersion relations derived from the Fourier analysis and theory. Béthune et al. (2021) performed 3D simulations using the PLUTO code to characterize these spiral wakes with pitch angles for given surface density profiles, and found that they corotate with the gas to a good approximation. They also found that non-local energy transport is negligible, with the angular momentum flux dominated by gravitational stresses having values close to  $\alpha$ -disks in equilibrium. A comparison and extrapolation of results from these rather expensive 3D simulations to our method of characterizing these spirals using a 2D cylindrical grid is a focus of this project. Our 2D simulations are comparably computationally inexpensive, allow much higher resolutions, and significantly reduce computational times.

The two-dimensional treatment of self-gravity comes with a caveat of typical disk height-to-distance ratios of  $\sim 0.05$  being too high for a thin disk approximation. This is treated by using a smoothing length  $\epsilon$  to smooth the gravitational accelerations, while also accounting for the vertical structure of the disk in order to match three-dimensional simulations. This was calculated by Müller et al. (2012), improved by Moldenhauer (2018) and is compatible with the FFT approach to obtain self-gravitational accelerations.

In Sect. 2 we cover protoplanetary disk physics, the conditions for gravitational instability and the related linear theory through a WKB analysis, and angular momentum transport. Our numerics and methods are covered in Sect. 3. We describe a few tests for our setup in Sect. 4. We report our findings and their implications in Sect. 5. We conclude with a discussion and summary of the results in Sects. 6.

## 2 Disk physics

In this section we are going to briefly summarize the equations governing protoplanetary disk hydrodynamics, and discuss the dynamics of a self-gravitating disk. We will also look at an overview of the thin disk approximation, vertical disk structure, linear theory and the associated dispersion relations for the GI, the WKB limit and the parametrized  $\beta$ -cooling mechanism.

### 2.1 Navier–Stokes equations

The density  $\rho$ , velocity  $\mathbf{v}$  and pressure  $P$  of the gas evolve according to the Navier–Stokes equations for mass, momentum and energy

$$\begin{aligned} \frac{\partial \rho}{\partial t} + \nabla \cdot (\rho \mathbf{v}) &= 0, \\ \rho \frac{\partial \mathbf{v}}{\partial t} + \rho(\mathbf{v} \cdot \nabla) \mathbf{v} &= -\nabla P - \rho \nabla \Phi, \\ \frac{\partial P}{\partial t} + \mathbf{v} \cdot \nabla P &= -\gamma P \nabla \cdot \mathbf{v} + Q_{\text{cool}}. \end{aligned} \quad (1)$$

We assume an ideal gas equation of state such that  $P = (\gamma - 1)\rho e$ , where  $e$  is the specific internal energy and  $\gamma$  is the adiabatic exponent. The isothermal sound speed is defined as  $c_{s,\text{iso}} = \sqrt{P/\rho}$  which in turn relates to the adiabatic sound speed  $c_{s,\text{ad}} = \sqrt{\gamma} c_{s,\text{iso}}$ . The term  $Q_{\text{cool}}$  in the energy equation represents radiative cooling, which we shall discuss in Sect. 2.6. The gravitational potential  $\Phi$  encompasses both the potentials of the central object and the self-gravitating disk. The potential at a distance  $r$  from the star can be written as  $\Phi_\star = -GM_\star/r$  where  $G$  is the gravitational constant and  $M_\star$  is the mass of the star. The potential of the disk satisfies the Poisson equation vanishing at infinity

$$\Delta \Phi_{\text{disk}} = 4\pi G \rho. \quad (2)$$

### 2.2 The thin disk approximation

Accretion disks are typically geometrically thin, that is, typical length scales in the vertical direction are small compared to the radial distance. The pressure scale height  $H$  is small compared to the cylindrical distance  $R$  from the star. AGN disks have aspect ratios  $h = H/R \approx 0.001\text{--}0.01$  and are comparatively thinner than protoplanetary disks with values of  $h \approx 0.03\text{--}0.1$  (Lodato, 2007). This thin disk approximation  $h \ll 1$  allows the integration of hydrodynamical equations in the vertical direction, allowing us to work with quantities per unit surface rather than volume. For example, the gas surface density  $\Sigma$  is defined as

$$\Sigma(R, \varphi) = \int_{-\infty}^{+\infty} \rho(R, \varphi, z) dz \quad (3)$$

The requirement of  $H/R \ll 1$  in length scales translates to the sound speed being much smaller than the rotational speed  $v_\phi$ , or  $c_{s,\text{iso}}/v_\phi = h \ll 1$ . The radial velocity  $v_r$  is much smaller than both  $c_s$  and  $v_\phi$  as accretion takes place on a long timescale (Lodato, 2007).

## 2.3 Vertical disk structure

The vertical disk structure of a non self-gravitating disk is derived using the hydrostatic balance between gravity and pressure with the assumption of a vertically isothermal gas ( $\partial c_s / \partial z = 0$ ). The solution to this is a Gaussian profile for  $\rho$  given a pressure scale height  $H_{\text{disk}} = c_{s,\text{iso}}/\Omega_K$ , where  $\Omega_K = \sqrt{GM_\star/R^3}$  is the Keplerian angular velocity

$$\rho(R, z) \approx \rho_{\text{mid}}(R) \exp\left(-\frac{z^2}{2H_{\text{disk}}^2}\right) \quad (4)$$

with  $\Sigma = \sqrt{2\pi}H_{\text{disk}}\rho_{\text{mid}}$ . In the limit where self-gravity dominates, the solution for the hydrostatic balance is a Spitzer profile (Spitzer, 1942) where the vertical surface density is given by

$$\rho(z) = \frac{\rho_0}{\cosh^2(z/H_{\text{sg}})} , \quad H_{\text{sg}} = \frac{c_{s,\text{iso}}^2}{\pi G \Sigma}. \quad (5)$$

This already hints towards the Toomre criterion discussed in Sect. 2.8, that is, self-gravity can be neglected in the regime where  $H_{\text{disk}}/H_{\text{sg}} \ll 1$ , implying

$$\frac{c_{s,\text{iso}} \Omega_K}{\pi G \Sigma} \gg 1. \quad (6)$$

More generally, including both contributions from the star and the disk complicates the vertical hydrostatic balance even further. There has not been an analytical solution derived for this case, but a simple interpolation formula (Bertin and Lodato, 1999) is used

$$H = \frac{c_s^2}{\pi G \Sigma} \left( \frac{\pi}{4Q^2} \right) \left[ \sqrt{1 + \frac{8Q^2}{\pi}} - 1 \right] = \frac{c_s^2}{\pi G \Sigma} f(Q). \quad (7)$$

## 2.4 The 2D equations

The vertically integrated 2D Navier–Stokes equations can now be derived based on the thin disk approximation and the description of the detailed vertical structure of the disk

$$\begin{aligned} \frac{\partial \Sigma}{\partial t} + \nabla \cdot (\Sigma \mathbf{v}) &= 0, \\ \Sigma \frac{\partial \mathbf{v}}{\partial t} + \Sigma(\mathbf{v} \cdot \nabla) \mathbf{v} &= -\nabla P_{2D} - \Sigma \nabla \Phi, \\ \frac{\partial P_{2D}}{\partial t} + \mathbf{v} \cdot \nabla P_{2D} &= -\gamma P_{2D} \nabla \cdot \mathbf{v} + Q_{\text{cool}} \end{aligned} \quad (8)$$

where  $\Sigma$  is the surface density as defined in Eq. (3) and the vertically integrated pressure is given by  $P_{2D} = (\gamma - 1)\Sigma e = R\Sigma T/\mu$ . Radiative cooling  $Q_{\text{cool}}$  is modeled as a local heat sink:

$$(\gamma - 1)Q_{\text{cool}} = \frac{P - \rho c_{\text{ref}}^2}{\beta \Omega_K^{-1}} \quad (9)$$

where  $\beta$  is a prescribed cooling parameter,  $\Omega_K$  is the Keplerian frequency, and  $c_{\text{ref}}$  is used to keep the disk aspect ratio from dropping too low. We use  $c_{\text{ref}}(R) = 0.001R\Omega_K$  in our simulations.

The contribution to the disk gravitational potential depends on the distribution through Eq. (2). The relation between surface density  $\Sigma$  and the disk gravitational potential  $\Phi_{\text{disk}}$  for an infinitesimally thin disk is given by elliptical integrals of the first kind,  $K$  and  $E$  ([Binney and Tremaine, 2011](#))

$$\frac{\partial \Phi_{\text{disk}}}{\partial R}(R, z) = \frac{G}{R} \int_0^\infty \left[ K(k) - \frac{1}{4} \left( \frac{k^2}{1 - k^2} \right) \left( \frac{R'}{R} \right) - \left( \frac{R}{R'} \right) + \left( \frac{z^2}{RR'} \right) E(k) \right] \sqrt{\frac{R'}{R}} k \Sigma(R') dR', \quad (10)$$

where  $k^2 = 4RR' / [(R + R')^2 + z^2]$ . This equation has analytical solutions only for particular interesting cases. One example would be the Mestel disk ([Mestel, 1963](#)) where  $\Sigma = \Sigma_0 R_0 / R$  and the disk extends to infinity, where the gravitational field takes the form

$$\frac{\partial \Phi_{\text{disk}}}{\partial R}(R) = 2\pi G \Sigma(R) \quad (11)$$

which turns out as the general solution for accretion disks in steady state in the limit of strong self-gravity ([Bertin, 1997](#)).

## 2.5 Centrifugal balance

Centrifugal balance requires the disk's angular velocity to be Keplerian, with  $\Omega \approx \Omega_K = \sqrt{GM_\star/R^3}$  at the lowest order. However, a small correction is introduced to include pressure gradients, that force the gas to move at sub-Keplerian speeds. In hydrodynamic equilibrium, the radial profile of azimuthal velocity  $v_\phi$  is given by

$$\frac{v_\phi^2}{R} = \frac{1}{\Sigma} \frac{\partial P_{2D}}{\partial R} + \frac{\partial \Phi_\star}{\partial R}. \quad (12)$$

Taking note of the corrections, we find that the deviation from Keplerian speeds relates to the disk aspect ratio and is of the order  $h^2$ . The angular velocity becomes

$$\Omega(R) = \Omega_K(R) \sqrt{1 + h^2 \frac{d \ln P_{2D}}{d \ln R}}, \quad (13)$$

giving sub-Keplerian rotation because in general  $P_{2D}$  decreases with radius. Adding self-gravity to the centrifugal balance alters Eq. (12) by a force term related to the disk gravitational

potential of the order  $GM_{\text{disk}}/R^2$  (Bertin and Lodato, 1999). For extremely massive protostellar disks, this term becomes dominant for rotation. For marginally gravitationally stable disks where  $Q \approx 1$ , deviation from the Keplerian motion is of the order  $h$ , stronger than the effect of pressure gradients (Kratter and Lodato, 2016).

## 2.6 $\beta$ cooling

As a cooling prescription, we use a parametrized mechanism introduced by Gammie (2001), and implement it similar to Sudarshan et al. (2022). The model assumes that any temperature change is relaxed to a reference profile  $T_0$  over a cooling timescale  $\tau = \beta\Omega_K^{-1}$  through the source term  $Q_{\text{cool}}$  such that

$$Q_{\text{cool}} = -\Sigma c_v \frac{T - T_0}{\tau} \Rightarrow \frac{\partial T}{\partial t} = -\frac{T - T_0}{\beta} \Omega_K, \quad (14)$$

where  $c_v = \mathcal{R}/\mu(\gamma-1)$  is the heat capacity at constant volume, with  $\mathcal{R}$  being the gas constant. This is identical to the modeling described in Eq. (9).

Such a prescription has a solution if viscous heating with  $Q_{\text{visc}} \approx \frac{9}{4}\nu\Sigma\Omega_K^2$  and the  $\alpha$ -viscosity model  $\nu = \alpha c_s H$  are included. Then, in steady state with no compressional heating ( $\nabla \cdot \mathbf{v} = 0$ )

$$Q_{\text{visc}} + Q_{\text{cool}} = 0 \Rightarrow T_{\text{eq}} = \frac{T_0}{1 - k\alpha\beta}, \quad k := \frac{9}{4} \sqrt{\gamma}(\gamma - 1) \quad (15)$$

with  $k \approx 1.06$  for  $\gamma = 7/5$ .

## 2.7 Dispersion relations

The properties of density wave propagation in a self-gravitating disk are understood through a linear perturbation analysis of the relevant hydrodynamic equations. This linear formalism involves the dispersion relation described by the radial and azimuthal wavenumbers  $(k, m)$ . For a sufficiently thin disk, the tight-winding limit of the WKB approximation becomes relevant and we have

$$\frac{dR}{d\phi} = -\frac{m}{k} = -R \tan(i), \quad (16)$$

which describes the structure of the spiral, with  $i$  being the pitch angle, or the angle between the spiral wavefront and a circle around the central object. This gives rise to the dispersion relation outlined in Cossins et al. (2009)

$$D(\omega, k, m) = (\omega - m\Omega)^2 - c_s^2 k^2 + 2\pi G \Sigma |k| - \kappa^2 = 0, \quad (17)$$

where  $c_s$  is the adiabatic sound speed and  $\Omega$  is the angular velocity. The perturbation behaves like a wave if  $\omega^2$  is positive for axisymmetric disturbances where  $m = 0$ . If  $\omega^2$  is negative, an instability arises that grows exponentially.

The dispersion relation gives rise to the Toomre criterion discussed in Sect. 2.8 when the right hand side of Eq. (17) is assumed to be positive definite; that is, the disk is gravitationally

unstable when the parameter  $Q \lesssim 1$ , and  $k_0 = \pi G \Sigma / c_s^2$  is the wavenumber most strongly excited. We also encountered this while discussing the vertical structure of the disk in Eq. (6). The relation can further be expressed using the pattern speed  $\Omega_p$ , where  $\omega = m\Omega_p$ , giving

$$m(\Omega - \Omega_p)^2 = c_s^2 \kappa^2 - 2\pi G \Sigma |k| + \kappa^2, \quad (18)$$

which also tells us that the excited modes must be close to the corotation  $\Omega \approx \Omega_p$ . Note, that  $k_0 = 1/h$  is exactly the inverse of the disk aspect-ratio. The 2D disk model, which requires  $k \ll 1/h$ , is well described by introducing the smoothing length that accounts for the vertical component of the disk gravity. Then the dispersion relation is given by,

$$m(\Omega - \Omega_p)^2 \simeq c_s^2 \kappa^2 - \frac{2\pi G \Sigma |k|}{1 + |k|/k_0} + \kappa^2, \quad (19)$$

which shifts the stability criterion from  $Q \lesssim 1$  to 0.647 but the modes are still corotating with the gas ([Bertin, 2014](#)).

A local dispersion relation can be established to explain the large-scale non-axisymmetric instabilities that occur even when  $Q > 1$  which is assumed to be stable in the WKB limit. This depends on a new parameter  $J$  ([Lodato, 2007](#)) in addition to  $Q$  where

$$J = m \left( \frac{\pi G \Sigma}{R \kappa^2} \right) \left( \frac{4\Omega}{\kappa} \right) \left| \frac{d \ln \Omega}{d \ln R} \right|^{1/2}, \quad (20)$$

where  $J$  is proportional to  $\Sigma$  and hence is a measure of the disk mass.

## 2.8 Toomre criterion

The stability criterion for a rotationally supported disk against self-gravity is given by the Toomre parameter ([Toomre, 1964](#))

$$Q = \frac{\kappa c_{s,\text{iso}}}{\pi G \Sigma}, \quad (21)$$

where  $\kappa$  is the epicyclic frequency and  $\Sigma$  is the vertically integrated gas surface density. As  $Q \rightarrow 1$ , self-gravity becomes prominent and, for  $Q \lesssim 1$ , the instability generates heat from the orbital energy via turbulence. We discuss the origins of the Toomre criterion in further sections.

One can express this constraint in the context of observations ([Kratter and Lodato, 2016](#)) where  $Q < 1$  translates to

$$\frac{M_{\text{disk}}}{M_{\star}} > 0.06 f \left( \frac{T}{10 \text{ K}} \right)^{1/2} \left( \frac{r}{100 \text{ au}} \right)^{1/2} \left( \frac{M_{\odot}}{M_{\star}} \right)^{1/2}. \quad (22)$$

Here,  $M_{\text{disk}}$  is the disk mass,  $M_{\star}$  is the mass of the star,  $T$  is the temperature,  $r$  is the disk radius and  $f$  is a prefactor of the order of unity that depends upon the surface density profile. This

sets a limit on the disk–star mass ratios of  $M_{\text{disk}}/M_{\star} \gtrsim 10^{-2}$  at which self-gravity becomes dominant.

## 2.9 Stresses and angular momentum transport

The accelerations associated with the self-gravitating potential play an important role in the transport of angular momentum in the disk. Perturbations in a turbulent disk give rise to torques that generate stress. This could be because of fluctuations in the flow velocity, magnetic fields, or the perturbed gravitational potential. For viscous disks, the popular  $\alpha$ -disk formalism ([Shakura and Sunyaev, 1973](#)) is used. The vertically integrated stress tensor  $T$  consists of just the shear term given by

$$T_{R\phi} = \alpha \Sigma c_s^2 \frac{d\ln\Omega}{d\ln R} \quad (23)$$

where  $\alpha$  is the dimensionless viscosity parameter, and the disk stress is closely associated with the local pressure. The factor  $d\ln\Omega/d\ln R = -3/2$  for Keplerian disks implies that the stress is negative, and acts against rotation allowing inward accretion.

The stress tensor for a self-gravitating disk then consists of two components; the Reynolds stress associated with fluctuations in the flow velocity components, and the gravitational stress arising from the perturbed gravitational potential. The Reynolds stress term is given by

$$R_{R\phi} = \rho(u_R - \langle u_R \rangle_\rho)(u_\phi - \langle u_\phi \rangle_\rho) \quad (24)$$

with velocity fluctuations in the  $R$  and  $\phi$  directions. Here,  $\langle u_R \rangle_\rho$  and  $\langle u_\phi \rangle_\rho$  are density-weighted vertical averages of the respective velocities. The gravitational stress is as described in [Lynden-Bell and Kalnajs \(1972\)](#) and given by

$$G_{R\phi} = \int \frac{g_R g_\phi}{4\pi G} dz, \quad (25)$$

where  $g_R$  and  $g_\phi$  are the accelerations due to the disk gravitational potential in the  $R$  and  $\phi$  directions. These stress tensor components, when normalized by the vertically integrated gas pressure  $P_{2D}$ , give the corresponding dimensionless viscosity components  $\alpha_R$  and  $\alpha_G$

$$\alpha = \alpha_R + \alpha_G ; \quad \alpha_R = \frac{R_{R\phi}}{P_{2D}}, \quad \alpha_G = \frac{G_{R\phi}}{P_{2D}}. \quad (26)$$

The balance between the heat dissipated as a result of the orbital energy extracted by the stresses against the  $\beta$ -cooling (denoted by LTE) uniquely determines a value of  $\alpha_{\text{LTE}}$  used by [Gammie \(2001\)](#). With our chosen normalization,

$$\alpha_{\text{LTE}} = \frac{1}{-\left(\frac{d\ln\Omega}{d\ln R}\right)(\gamma - 1)\beta} \quad (27)$$

where  $\beta$  is a cooling parameter. Standard wave mechanics link energy and angular momentum

density of the density waves to the square root of the perturbed gas surface density. Thermal regulation requires the instability to saturate at an amplitude that scales as the square root of the cooling time with

$$\frac{\Delta\Sigma}{\Sigma} \propto \frac{1}{\sqrt{\beta}}. \quad (28)$$

This behavior was confirmed by [Cossins et al. \(2009\)](#). This has implications on the fact that the strength of the instability depends upon the thermodynamics at steady state.



## 3 Numerics

In this section, we outline the numerical methods used in the project: the GPU self-gravity module and the 2D self-gravity approximation. We also describe the computational domain, the initial and boundary conditions, methods of integration and the model parameters of our setup.

### 3.1 Implementing self-gravity

The gravitational potential of the disk satisfies the Poisson equation (refer to Eq. (2)) and is numerically solved using a Poisson solver in the computational domain with appropriate boundary conditions. [Béthune et al. \(2021\)](#) used a method that treats the equation as a matrix inversion problem. The Laplacian operator was discretized in spherical geometry using a second-order finite-difference scheme and the gravitational potential was solved for every hydrodynamical time-step.

The potential can be written as a convolution product ([Binney and Tremaine, 1987](#)), enabling the calculation of the gravitational accelerations using Fast Fourier Transforms (FFTs). The accelerations can also be written as a convolution product, skipping the calculation of the derivatives of the potential itself ([Baruteau, 2008](#)). This is the idea behind the Poisson solver we use.

#### 3.1.1 The 2D self-gravity approximation

The discretized gravitational potential in 3D is given by

$$\Phi_{3D}(\mathbf{r}) \simeq -G \sum_{\mathbf{r}'} \frac{\rho(\mathbf{r}') \Delta V'}{\sqrt{(\mathbf{r} - \mathbf{r}')^2 + \varepsilon_{3D}^2}} \quad (29)$$

where  $\Delta V'$  is the volume of the cell located at  $\mathbf{r}'$ . The smoothing potential  $\varepsilon_{3D}$  took care of the  $\mathbf{r} = \mathbf{r}'$  divergence and the finite volume in the computational domain. With a known vertical distribution and surface density, the 2D potential is obtained by integrating Eq. (29) in the vertical direction

$$\Phi_{2D}(\mathbf{r}) = \int \Phi_{3D}(\mathbf{r}) \rho(z) dz. \quad (30)$$

Using the razor thin disk approximation and approximating the vertical profile with a delta function, we can write the 2D potential with a smoothing length  $\varepsilon_{2D}$

$$\Phi_{2D}(r, \phi) = -G \sum_{r', \phi'} \frac{r' \Sigma(r', \phi')}{\sqrt{s^2 + \varepsilon_{2D}^2}} \Delta r' \Delta \phi' \quad (31)$$

where  $s = \sqrt{r^2 + r'^2 - 2rr'\cos(\phi - \phi')}$ . The accelerations are given by the gradient of the potential  $\mathbf{g} = -\nabla_r \Phi$ . A commonly used smoothing length  $\varepsilon_{2D}(\mathbf{r}, \mathbf{r}') = B^2 r^2$  fits into the form that allows accelerations to be written as convolution products. However, it was found that the

2D approximation with this smoothing length overestimates the gravitational accelerations and the condition also violates Newton’s third law. [Moldenhauer \(2018\)](#) improved the smoothing length to be compatible with 3D simulations with  $\varepsilon_{2D}(\mathbf{r}, \mathbf{r}') = \chi^2 rr' + \lambda^2(r - r')^2$ , where  $\chi, \lambda$  are parameters that are determined using a suitable vertical profile for the disk.

### 3.1.2 The GPU-CUDA self-gravity module

PLUTO ([Mignone et al., 2007](#)) is a grid-based code used to simulate complex astrophysical flows. We use the GPU version of PLUTO 4.2 developed by [Thun and Kley \(2018\)](#). The 2D self-gravity algorithm was implemented into the aforementioned version of the code in [Moldenhauer \(2016\)](#), which follows the implementation in FARGO–ADSG [Baruteau \(2008\)](#). The constant smoothing length was later modified with the variable one described in the section above.

## 3.2 Domain and integration scheme

We used cylindrical polar coordinates, with  $N_R \times N_\phi = 518 \times 512$  which corresponds to  $\sim 7$  cells per scale height (cps) in  $R$  and  $\sim 4$  cps in  $\phi$  for our normal resolution runs. The radial domain extends from  $1\text{--}1/32 R_0$  with logarithmic spacing. These values are chosen for comparison of resolution studies with [Béthune et al. \(2021\)](#). We also ran a few models with double resolution.

We integrate the Navier–Stokes equations in Eq. (8) with RK2 (second-order Runge–Kutta) time-stepping. We use a linear reconstruction scheme ([Harten, 1983](#)) with a van Leer slope limiter ([Van Leer, 1974](#)). We used the HLLc Riemann solver ([Toro et al., 1994](#)) with a Courant–Friedrichs–Lewy (CFL) condition of 0.3. The gravitational potential of the star is included with the NBody module by [Thun and Kley \(2018\)](#).

## 3.3 Initial and boundary conditions

We initialize our setup with equilibrium power-law profiles for the surface density  $\Sigma(R)$  and temperature  $T(R)$ . The velocity component  $v_R$  is set to zero, and  $v_\phi(R)$  is set to the Keplerian velocity corrected for pressure support through Eq. (13). In order to maintain a constant aspect ratio with the Keplerian frequency being  $\Omega_K \sim R^{-3/2}$ , the sound speed is set to  $c_s \sim R^{-1/2}$ . We started near  $Q = 1$  to avoid the initial long cooling, which implied a gas surface density of  $\Sigma \sim R^{-2}$ .

The inner radial boundary is reflective (we symmetrize  $\Sigma$ ,  $P$ , antisymmetrize  $v_R$  and set  $v_\phi$  to Keplerian), and the outer boundary is set to outflow (zero gradient across the boundary). The azimuthal boundary is periodic. We impose a density floor of  $10^{-9}\Sigma_0$ , and we also use an  $h_{\text{floor}} = 10^{-3}$  to avoid negative temperatures.

We use the prescription detailed in [de Val-Borro et al. \(2006\)](#) to damp the inner and outer

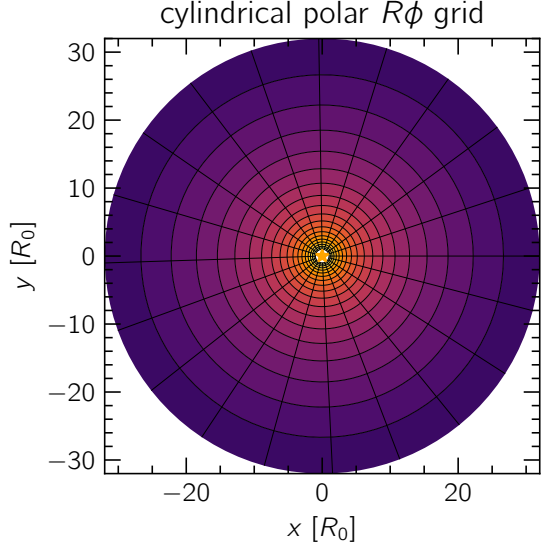


Figure 2. A representation of our grid setup in  $R\phi$  coordinates with logarithmic spacing in  $R$ . The contour represents a radially dropping surface density profile  $\Sigma(R)$ .

radial zones, that is,  $R < 1.2 R_0$  and  $R > 30 R_0$  respectively with the following equation:

$$\frac{\partial x}{\partial t} = -\frac{x - x_0}{\tau_{\text{damp}}} f(r) \quad (32)$$

where  $x$  refers a physical parameter ( $\Sigma, \mathbf{v}$ ),  $\tau$  is the damping time at the boundaries and  $f(r)$  is a parabola used to smoothly connect the damping zone to the active domain's internal boundary. We choose a damping time of  $\tau = 0.1 t_0$  where  $t_0 = 2\pi/\Omega_K$  in our models. We note that damping at the boundaries does not conserve mass and might have an effect on the total mass in the computational domain. On close observation, we saw that the total disk mass roughly varies by a factor of 2% every 1000 orbits.

### 3.4 Units and model parameters

All the quantities are modeled in code units allowing our models to be scaled freely. We measure masses with respect to the central object  $M_\star$ . The length unit chosen is the inner radial boundary  $R_0$ . We chose the time unit to be in terms of the inner orbital period with  $t_0 = 2\pi/\Omega_K$ .

We define disk masses as a fraction of the central star mass, the values of which are described in Table 1 below, and the cooling timescale defined through the dimensionless parameter  $\beta$ . We also initialize the disk aspect ratio  $h = H/R$  where  $H$  is the pressure scale height. We use a  $\gamma = 5/3$ . In addition, we ran the models M5B10 and M10B10 in double resolution with  $N_R \times N_\phi = 1024 \times 1036$ , and the M2B10 module with low  $\beta$  values of 1 and 3 to check for fragmentation.

Model	$q = M_{\text{disk}}/M_{\star}$	$\beta$	$h$
M1B10	1	10	0.1
M2B10	1/2	10	0.064
M3B10	1/3	10	0.045
M5B10	1/5	10	0.028
M10B10	1/10	10	0.014
M3B32	1/3	$10^{3/2}$	0.041
M3B100	1/3	100	0.044

Table 1. List of parameters for all our 2D models. We describe the name of the model, the disk mass as a fraction of the central object mass  $q$ , the value of  $\beta$ , and the initial aspect ratio  $h$ . These models were chosen with parameters from [Béthune et al. \(2021\)](#) to provide a detailed comparison between the 3D and 2D models.

### 3.5 On the indirect term

[Béthune et al. \(2021\)](#) assumed an inertial reference frame whereas we include the indirect term, that is, the net force on the central object from the disk. We note that the effect of this indirect term is negligible for our analysis ([Michael and Durisen, 2010](#)) but is included for correctness. Figure 3 shows the center-of-mass trajectory of the central object reacting to disk self-gravity with the indirect term included.

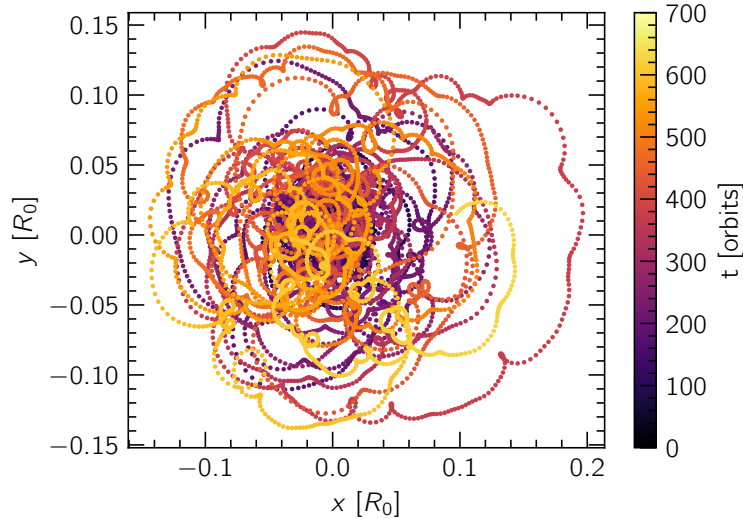


Figure 3. The trajectory of the center of mass for the run M5B10 in our models. The color represents the time in orbits. The trajectory remains well within the inner boundary  $R/R_0 < 1$ , showing that the disk remains largely undisplaced.

### 3.6 Computing turbulent stresses

In this section, we outline the method to compute the Reynolds and gravitational stresses defined in Sect. 2.9. We follow the approach in [Balbus and Papaloizou \(1999\)](#) to treat flow

quantities that are azimuthally averaged as radially smooth functions. The density-weighted mean of a quantity  $F$  is then defined as

$$\langle F \rangle_\rho = \frac{1}{2\pi\Sigma\Delta R} \int_{R-\Delta R/2}^{R+\Delta R/2} \int_0^{2\pi} \Sigma F dR d\phi \quad (33)$$

We first compute time-averaged disk quantities spanning a number of files after a timestamp at which GI saturation is achieved using the last 300 files at intervals of one orbit at  $R_0$ . Now, we compute the Reynolds stress at file index  $i$ ,

$$R_{R\phi}^i = \Sigma^i (u_R^i - \langle u_R^i \rangle_\rho) (u_\phi^i - \langle u_\phi^i \rangle_\rho). \quad (34)$$

The gravitational stress is also computed with a midplane density normalization of  $\sqrt{2\pi}H$  for the vertical length scale,

$$G_{R\phi}^i = \int \frac{g_R^i g_\phi^i}{4\pi G} dz = \frac{g_R^i g_\phi^i}{4\pi G} \times \sqrt{2\pi}H^i \quad (35)$$

We time-average both stress quantities over  $N$  files to compute the mean,

$$\bar{X}_{R\phi} = \frac{1}{N} \sum_i^N X_{R\phi}^i(R) \quad (36)$$

where  $\bar{X}_{R\phi} = \{\bar{R}_{R\phi}, \bar{G}_{R\phi}\}$ . We then radially smooth the stresses and pressure, and obtain the stress coefficients  $\alpha_R$  and  $\alpha_G$  by normalizing the stresses with the vertically integrated, azimuthally averaged pressure  $P_{2D}$ .



## 4 Tests

We include the results of some test models in this section. We test the GPU self-gravity module with a point mass inside our domain, the  $\beta$ -cooling prescription with a simple Keplerian disk in 1D, and our model setup in 1D without self-gravity.

### 4.1 Self-gravity: potential of a point mass

For a given density distribution  $\sigma(\mathbf{r})$  at location  $\mathbf{r}$ , the gravitational potential is given by the integral

$$\Phi(\mathbf{r}) = - \int_{V'} \frac{G}{|\mathbf{r} - \mathbf{r}'|} \sigma(\mathbf{r}') dV', \quad (37)$$

where  $dV'$  is the Euclidean volume element. The gravitational potential  $\Phi$  from the Green's function corresponding to the Poisson equation for a point mass  $m$  at a distance  $\mathbf{r}$  and the corresponding acceleration  $\mathbf{a}$  in three dimensions are

$$\Phi(\mathbf{r}) = -\frac{Gm}{r}, \quad \mathbf{a}(\mathbf{r}) = -\nabla\Phi = -\frac{Gm}{r^3}\mathbf{r}. \quad (38)$$

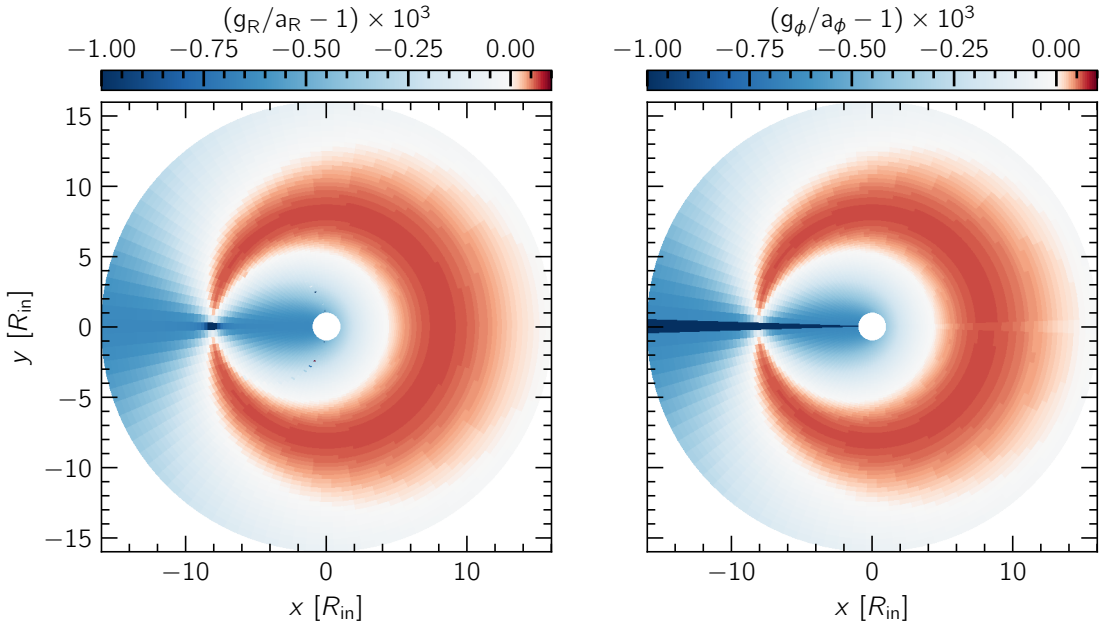


Figure 4. The gravitational accelerations  $g_R$  and  $g_\phi$  from the GPU self-gravity module are plotted with respect to the analytically calculated accelerations  $a_R$  and  $a_\phi$  for a point mass. They fall within an error margin  $\leq 10^{-3}$ . The point mass is centered at around  $(x, y) = (-R_0, 0)$ , as visible in the figure.

We prescribed a surface density profile for a point mass  $m$ , located at a grid cell  $R = R_0$  and  $\phi = \phi_0$  as a Dirac delta function with a floor:

$$\sigma = \max(\delta(R_0, \phi_0), 10^{-10}) = \begin{cases} 1 & \text{if } R = R_0 \& \phi = \phi_0 \\ 10^{-10} & \text{otherwise} \end{cases} \quad (39)$$

The delta function is centered around a cell at  $R_0 = 8R_{\text{in}}$  and  $\phi = \pi$  with 100 cells in  $R$  between  $1-16R_{\text{in}}$  and 101 cells in  $\phi$ . The gravitational accelerations  $g_R$  and  $g_\phi$  obtained are plotted with respect to the analytical solution in Fig. 4. We recover the analytical solution with an acceptable margin of error, verifying the accuracy of the GPU self-gravity module.

## 4.2 Testing $\beta$ cooling

We tested our  $\beta$ -cooling prescription with a one-dimensional disk without self-gravity. We set up a disk with 200 cells in  $R$  using the initial and boundary conditions described in Sect. 3.3 and an  $\alpha$ -viscosity prescription with  $\alpha = 0.1$ . We use a cooling parameter  $\beta = 1$ . The analytical solution for the equilibrium temperature in steady state with no compressional heating is given by Eq. (15). We plot the radial profile of temperature against this analytical solution in Fig. 5. We see that the temperature profile reaches the analytical solution with time.

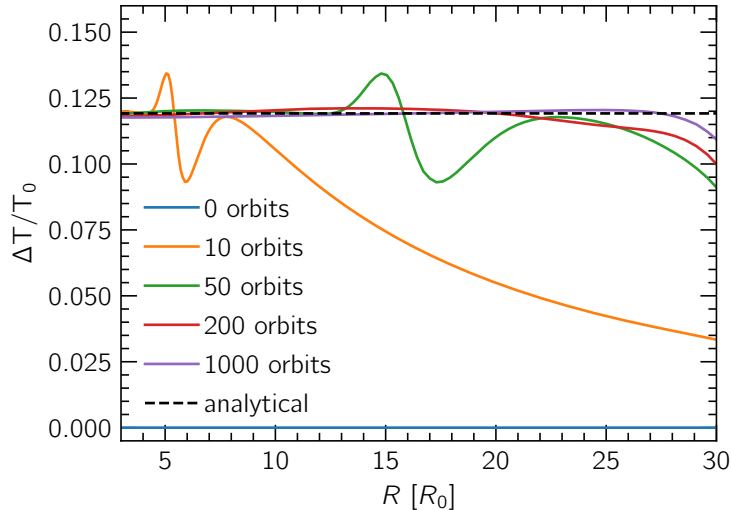


Figure 5. The temperature deviation from the initial profile is plotted against the radial distance. The dashed line denotes the expected profile from Eq. (15). We plot for various times  $t = 0, 10, 50, 200$  and  $1000$  orbits.

## 4.3 A stable 1D disk

We tested our M2B10 model setup in one dimension with 518 cells in  $R$  without self-gravity to check if the disk remains stable over time. Fig. 6 shows a plot of surface density fluctuations

$\Delta\Sigma/\Sigma_0$  in time. We see that the profile stays constant, concluding that our setup is stable in 1D without self-gravity. We now move ahead to 2D models, which are described in the next section.

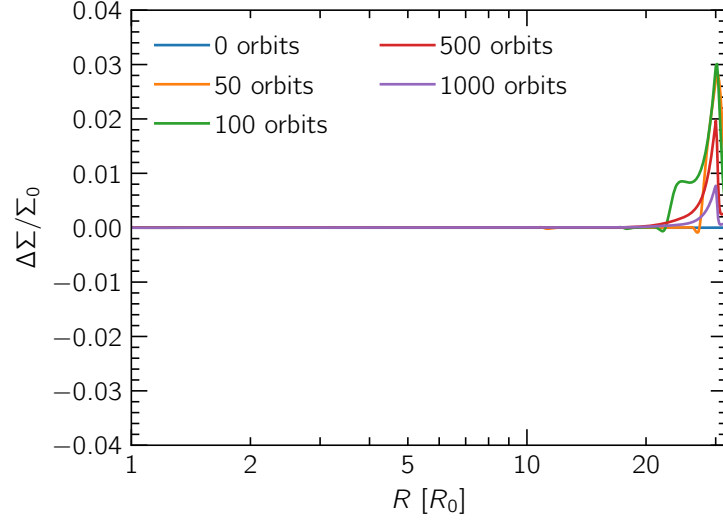


Figure 6. The surface density deviation from the initial profile is plotted against the radial distance. We plot for various times  $t = 0, 50, 100, 500$  and  $1000$  orbits.



## 5 Results

In this section, we outline the results of our simulations. We first describe the evolution and features, and evaluate disk quantities for an example simulation. We tie the results of all our models together in the next subsection, and further compare them to previous 3D simulations. Finally, we highlight the effects of resolution, and discuss disk fragmentation for disks with fast cooling.

### 5.1 A reference simulation

In Sect. 2.8, we discussed the disk–star mass ratios where self-gravity becomes important. Here, we begin by describing different features seen in our reference simulation M5B10 with disk mass  $M_{\text{disk}} = 1/5M_{\star}$  which is a modest upper limit to observed disks, and a cooling parameter  $\beta = 10$ . We outline the results for the other models in our parameter space (refer to Table 1) in the following sections.

#### 5.1.1 Illustration of the disk evolution

In Fig. 7, we lay out the evolution of our disk in time sampling  $t = 50, 200$ , and  $500$  orbits. We see that the gas surface density shows spiral features in the inner parts of the disk after  $50$  orbits. The mass redistribution throughout the radial domain of the disk takes several hundred orbits and we see that the GI reaches a fully developed state at  $500$  orbits. The interplay between cooling and turbulence due to the GI lead the system to a saturation state.

This is also clearly depicted in the time evolution of the azimuthally averaged gas surface density relative to its initial profile, shown in Fig. 8. The non-quasi steady initial conditions show a short-lived transition, but we see the stripes of axisymmetric density perturbations

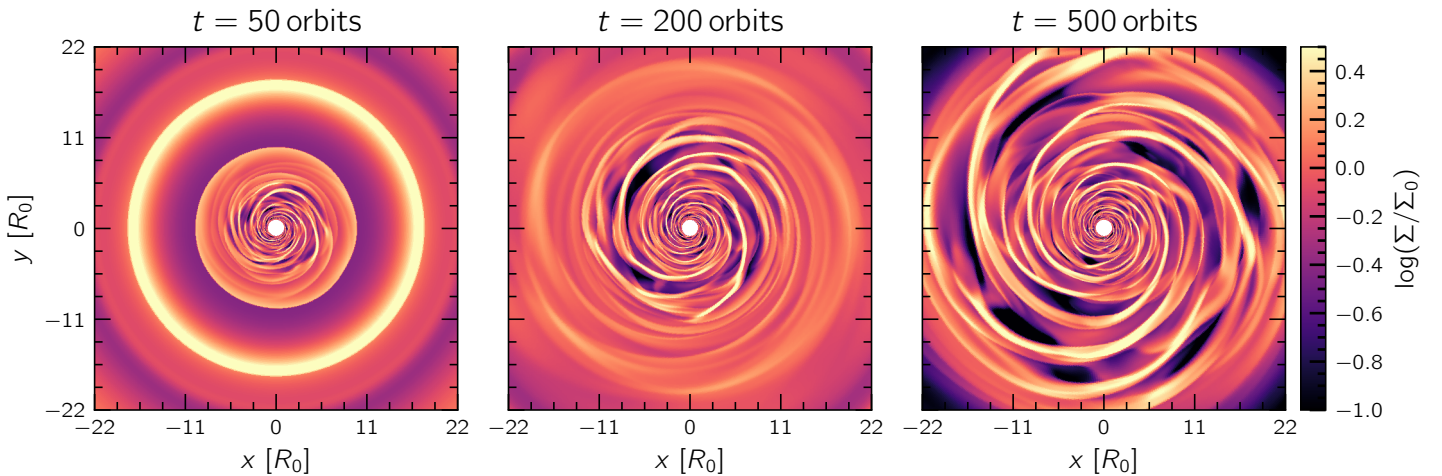


Figure 7. Two dimensional snapshots of gas surface density normalized to its initial profile from the M5B10 model at various timestamps  $t = 50, 200$  and  $500$  orbits. The mass redistribution stabilizes at  $t = 500$  orbits.

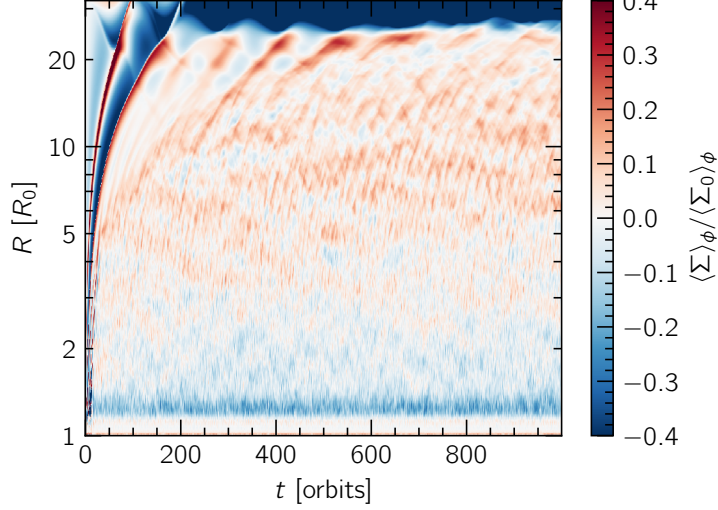


Figure 8. Time evolution of the radial map of the azimuthally averaged gas surface density normalized to its initial profile.

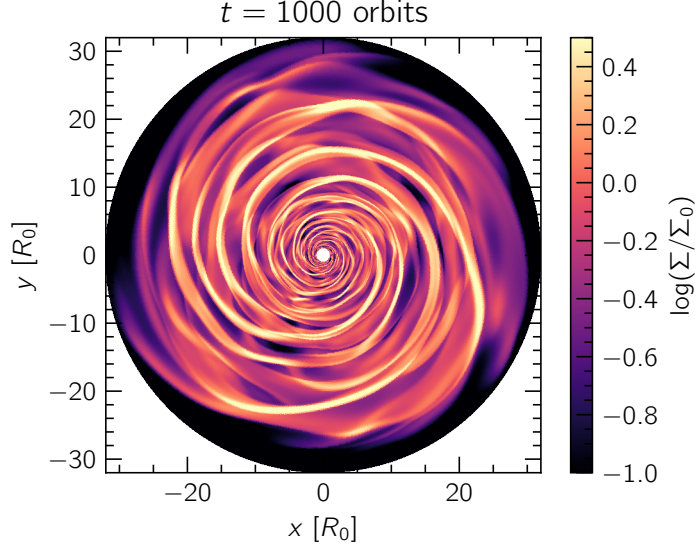


Figure 9. A 2D snapshot of the fully-developed gas surface density  $\Sigma$  normalized to its initial profile for the model M5B10 at time  $t = 1000$  orbits. The relative surface density extends roughly about 1.5 orders in magnitude.

traveling at roughly Keplerian speeds. We see that the gas surface density decreases at the inner radii and increases at the outer radii.

### 5.1.2 Flow features

Figure 9 shows the ubiquitous spiral arm structure in the gas surface density with relatively tight winding. The disk is non-axisymmetric, and we see large trailing (oriented against the direction of rotation) spiral arms that span several radii from their excitation point. We can

clearly identify that the spirals are self-similar and have constant pitch angles radially.

The radial velocity profile normalized to the azimuthally averaged sound speed in the  $R\phi$  plane is illustrated in Fig. 10. We see that the flow alternates between sub- and super- sonic behavior at a given radius. The inward and outward fluctuations, both at small and large scales, are similar in magnitude. The y axis representing the radial distance in the figure is logarithmically spaced indicating that these perturbations show up in a logarithmic fashion. The spirals are oriented where there is a radial velocity jump (blue to red), that is, where  $v_R$  flips sign. The 2D snapshot at  $t = 1000$  orbits does show signs of a global pattern for the spiral but one would have to look at how the fluctuations evolve in time to get a clear picture. These midplane compressions are expected to likely cause vertical outflows in 3D simulations (Béthune et al., 2021).

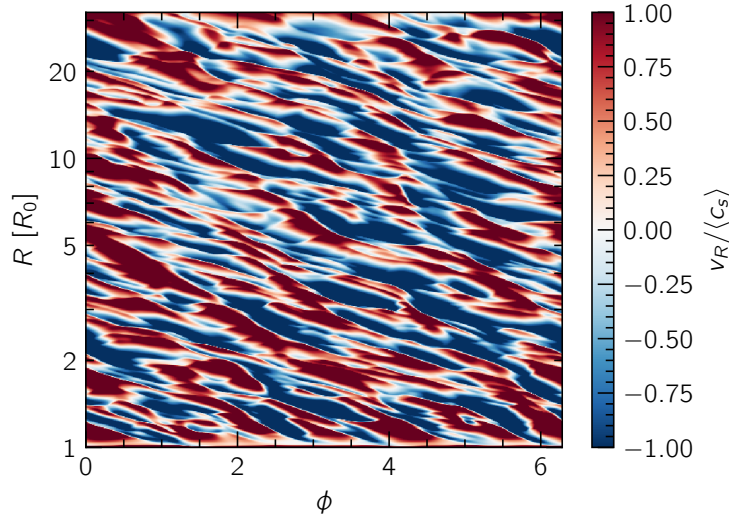


Figure 10. A 2D snapshot of the radial velocity normalized to the azimuthally averaged sound speed in the  $R\phi$  plane. The flow shows sub- (blue) and super- (red) sonic behavior.

### 5.1.3 The Toomre parameter

To see how the gravitational instability manifests itself, we measure the Toomre parameter  $Q$  as illustrated in Eq. (21). We estimate the epicyclic frequency  $\kappa$  using the density-weighted orbital velocity  $\langle \Omega \rangle_\rho = \langle v_\phi / R \rangle_\rho$  with

$$\kappa \approx \sqrt{\frac{2\langle \Omega \rangle_\rho}{R} \frac{dR^2 \langle \Omega \rangle_\rho}{dR}}. \quad (40)$$

The profiles of  $Q$  are density-weighted for a few instances in time and depicted in Fig. 11. The dashed line represents the condition for marginal gravitational stability  $Q \approx 1$ . We clearly see that the disk self-regulates to marginal stability and conclude that GI turbulence is the most

dominant effect. The orbital energy extracted into heat, which counteracts cooling, would cause the angular momentum flux to depend on our cooling parameter ([Gammie, 2001](#)), which is further studied in Sect. 5.1.5.

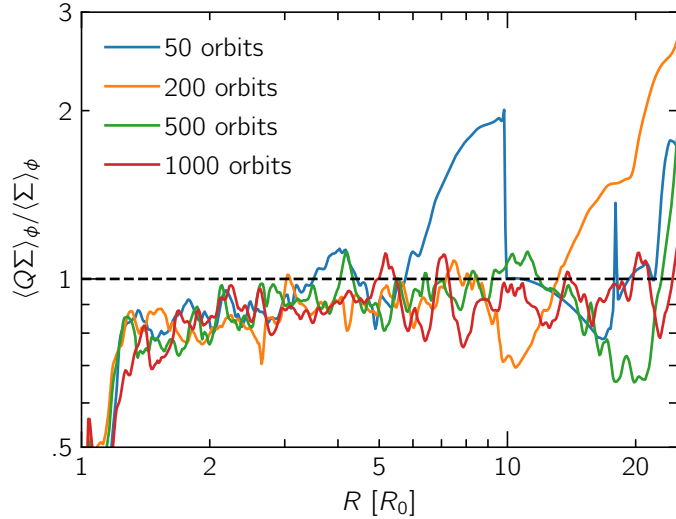


Figure 11. Radial profile of the density-weighted Toomre parameter  $Q$ . We plot for various times  $t = 0, 50, 200, 500$  and  $1000$  orbits. The dashed line represents marginal stability at  $Q \approx 1$ .

There are other instabilities that could exist in tandem with the saturation of GI which we ignore in the context of our simulations ([Béthune et al., 2021](#)). However, we explore the possibility of a parametric instability to explain the gravitational stresses between our normal to double resolution runs in the following sections.

#### 5.1.4 On the disk aspect ratio

The disk settles to an aspect ratio  $h$  predicted by the marginal stability condition once it reaches a quasi-steady state, given by

$$h = \frac{H}{R} \approx \frac{\pi R^2 \Sigma(R)}{M_\star} \quad (41)$$

Figure 12 shows the azimuthally averaged, density-weighted aspect ratio profiles at different times. We see that  $h$  converges to the expected value 0.028 indicated by the dashed line as seen in the 3D simulations in [Béthune et al. \(2021\)](#). In addition, we observed that the choice of our outflow initial condition at the outer boundary significantly improved the convergence to the expected value whereas there was a larger degree of fluctuations with our previously used reflective outer boundary.

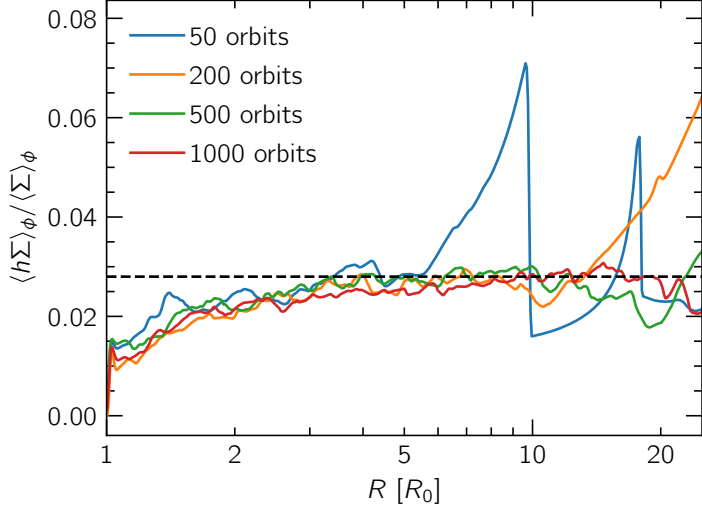


Figure 12. Density weighted aspect ratio  $h$  against the radial distance at different times  $t = 50, 200, 500$  and  $1000$  orbits. The dashed line represents the value  $0.028$  from the 3D simulations of [Béthune et al. \(2021\)](#)

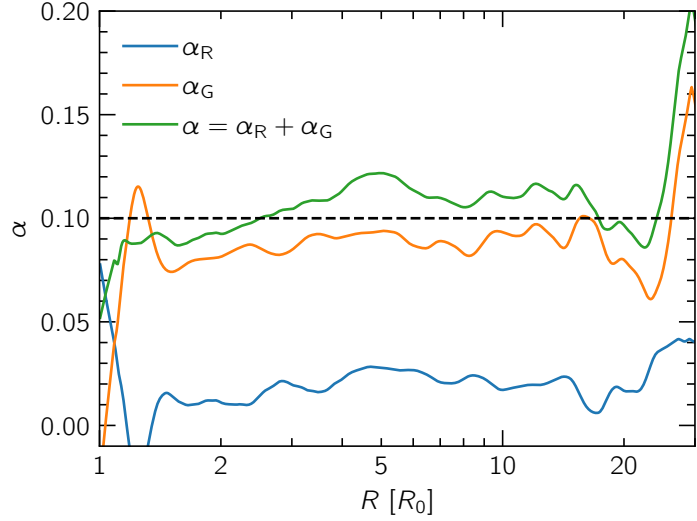


Figure 13. Radial profiles of the Reynolds (blue), gravitational (orange) and the total stress (green) after time and azimuthal averaging over 200 orbits, and radial smoothing for the run M5B10. The dashed line indicates the expected value  $\alpha_{\text{LTE}}$  calculated using Eq. (27).

### 5.1.5 Stresses

The equation of angular momentum governs mass accretion. The radial flux of angular momentum for a self-gravitating disk consists of a contribution from the Reynolds stress and the gravitational stress, as discussed in Sect. 2.9. Thermal balance between the orbital energy extracted from the stress as heat and  $\beta$ -cooling determines a value  $\alpha_{\text{LTE}} \approx 0.1$  for a  $\beta = 10$ . Figure 13 shows the time-averaged (over 200 files), and radially smoothed stress profiles for the model M5B10. The method used to compute these stresses is outlined in Sect. 3.6. The

net contribution from both Reynolds and gravitational stresses is positive and shows some oscillation about a mean value which sufficiently matches the  $\alpha_{\text{LTE}}$  assuming a Keplerian shear rate, with an error bar of  $10^{-2}$ . In the figure,  $\alpha_{\text{LTE}}$  is denoted by the black dashed line. We see that the total stress is dominated by self-gravity, with values of the order  $\alpha_G \approx \alpha$ , while the hydrodynamical Reynolds stress oscillates around a value  $\alpha_R \approx 0.02$ . We can say that the transport of angular momentum is thus governed by the contribution from gravitational accelerations. We will later show that the value of stress is resolution-dependent.

### 5.1.6 Pitch angle of the spirals

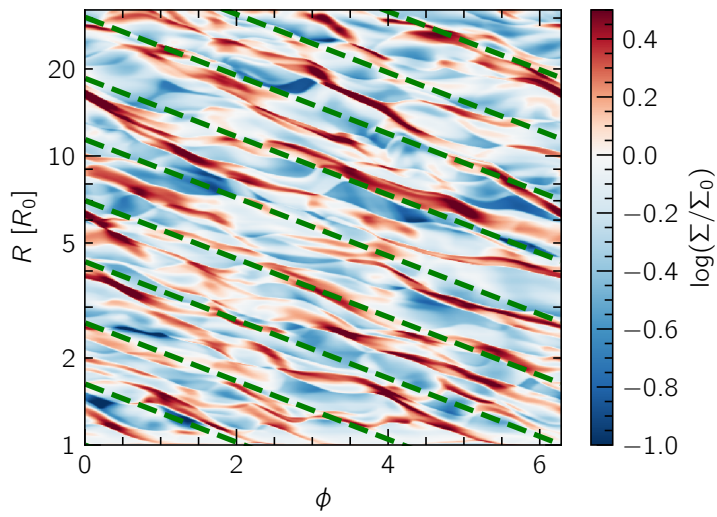


Figure 14. Two-dimensional density fluctuations in the  $R\phi$  plane for the M5B10 model at  $t = 1000$  orbits. The dashed diagonal lines fit the spirals and the slope of the family of lines is the mean pitch angle  $\tan(i) = 0.232$ , or  $i = 13.06^\circ$ .

We plot the relative density fluctuations in the  $R\phi$  plane for the run M5B10 in Fig. 14. Peaks in the gas surface density correspond to when the radial velocity undergoes a sign change as depicted clearly in Fig. 10. The pitch angle  $i$  is closely connected to the spiral radial and azimuthal wavenumbers through the dispersion relation Eq. (16). We see that all spirals share similar pitch angles throughout the disk. Thus, for pitch angles independent of  $R$ , we can fit these spirals with a family of lines  $\log R = -\tan(i)\phi + c$ . To determine the value  $i$ , we made a mean linear fit with the lines and calculated the slope. We did this by visually fitting each line, but this is also more rigorously done using an autocorrelation of the relative density fluctuations, determining how two points in the  $(\log R, \phi)$  space are correlated. We found the mean value of  $i$  to satisfy  $\tan(i) = 0.232$ , corresponding to an  $i = 13.06^\circ$ . The range of pitch angles determined with our models were found to be around 4–5 times larger than pitch angles measured in non-selfgravitating disks by Ogilvie and Lubow (2002) which are a result of tidal density fluctuations. The spirals have similar pitch angles independent of radius or time, and either propagate without shearing or they form and dissipate intermittently within a short wavenumber range.

### 5.1.7 Dispersion relations

With the pitch angles obtained from Sect. 5.1.6, we can now determine the radial and azimuthal wavenumbers of the spirals from the dispersion relation. We calculated the density weighted average wavenumber  $k_0 \approx \pi G \Sigma / \langle c_{s,\text{iso}} \rangle_\rho^2$ , discussed in Sect. 2.7, that is most strongly influenced by self-gravity. With the obtained  $k_0$ , the linear, two-dimensional waves have a predicted azimuthal wavenumber of  $m_0 = k_0 R \tan(i)$ . For our run M5B10, we found that the calculated wavenumber is of the order  $m_0 \approx 9.8 \pm 1.04$ . We identified spirals of the order  $m = \{5, 7\}$  in the azimuthal slices of gas surface density. This is, under a reasonable error bar, close to the result found in [Béthune et al. \(2021\)](#) where they report a  $m \approx m_0/2$ .

## 5.2 Parameter survey

After having provided an outline of the reference simulation in our previous section, we now start comparing it to the models in the rest of our parameter space, described in Table 1. The sections outlined below tie our results together for different cooling parameters  $\beta$  and star–disk mass ratios  $q = M_{\text{disk}}/M_{\star}$ .

### 5.2.1 Comparison of 2D surface densities

Figure 15 shows the 2D surface density normalized to its initial profile for models with a constant cooling parameter  $\beta$  and different star–disk mass ratios  $q$ . With increasing disk masses, we see that the radial wavelength of the instability goes up. This is a result of the quadratic dispersion relation in Eq. (18), which predicts the prominent wavelength of the instability  $k_0$  to be inversely proportional to the disk aspect ratio.

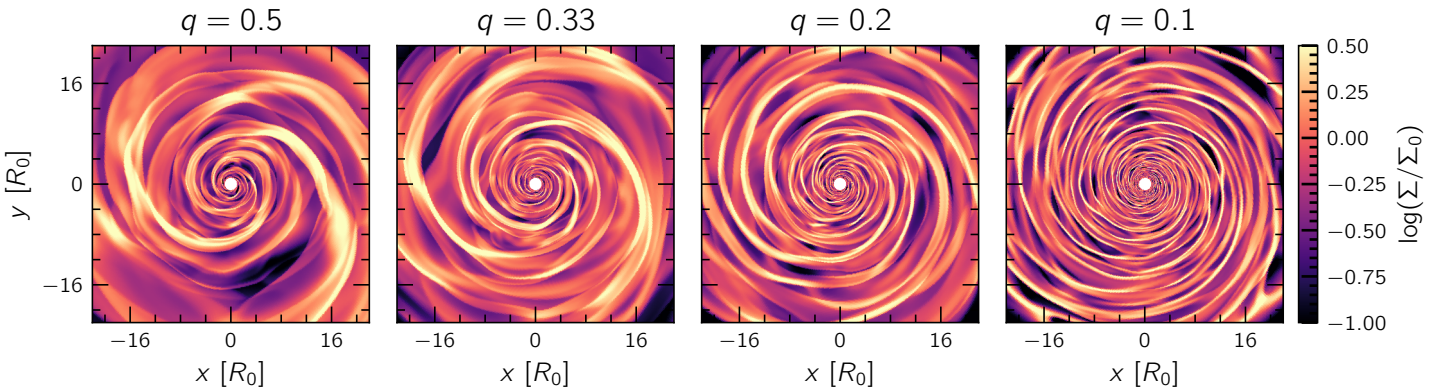


Figure 15. Comparison of two dimensional snapshots of gas surface density normalized to its initial profile from the runs M2B10, M3B10, M5B10, M10B10 at time  $t = 1000$  orbits. As disk mass decreases, we see more densely packed spirals.

We clearly see how the number of spirals differs with respect to  $q$ . The first two panels—each with  $q = 1/2$  and  $q = 1/3$ —show fewer, thicker and more open spirals but as  $q$  decreases, we see more and sharper spirals. At first glance, a global pattern is hard to identify with the 2D plots corresponding to runs M2B10 and M3B10. But as we already saw for M5B10 and M10B10, the spirals show self-similarity and orient themselves with similar pitch angles radially. We also see a clear variation of the radial wavenumber depending on  $q$ .

With Fig. 16 we illustrate the variation of the 2D surface densities with respect to different cooling parameters  $\beta = 10, 10^{3/2}$ , and 100. We see that models with a larger cooling timescale take a very long time to reach equilibrium. Model M3B32 took roughly 2600 inner orbits to show a fully-developed spiral structure in the domain whereas we see that run M3B100 with  $\beta = 100$  is not in steady state even after 7000 orbits. We ran this model with a lower resolution of  $N_R \times N_\phi = 128 \times 128$  and found that it does settle into spirals in steady state, but there was an  $m = 2$  mode developing in the normal resolution run at about 10000 orbits.

Cossins et al. (2009) show that the radial spiral wavenumbers vary with respect to the chosen cooling parameter. This finding, although visually not apparent, is true for our models with  $\beta = 10$  and  $10^{3/2}$ .

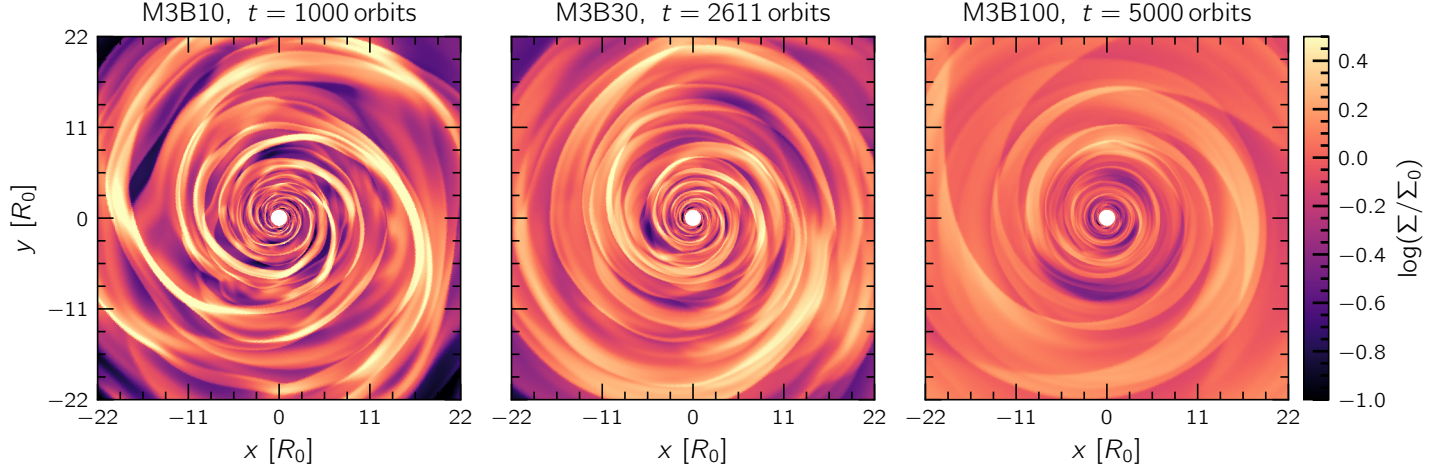


Figure 16. Comparison of 2D snapshots of gas surface density normalized to its initial profile from models M3B10, M3B32, M3B100 at timestamps  $t = 1000, 2611$  and  $5000$  orbits respectively.

### 5.2.2 High disk mass case: $q = 1$

We find that the system becomes highly unstable for the case where the disk is as massive as the star ( $q = 1$ ) and all the material is lost from the domain once the model reaches 600 orbits.

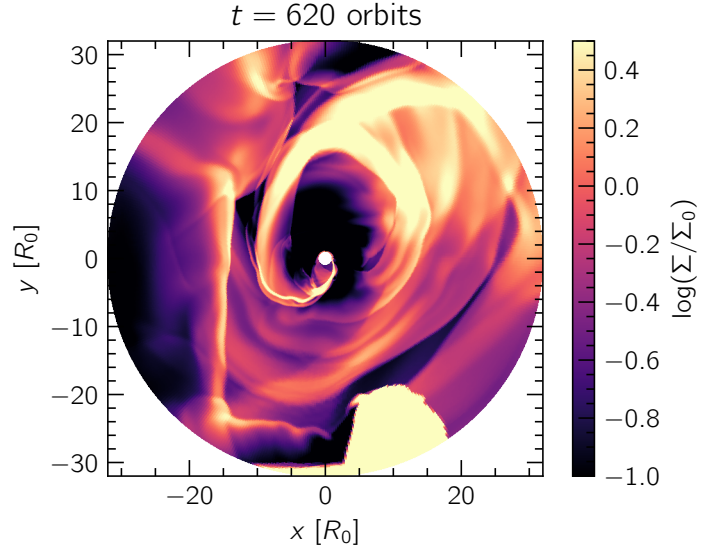


Figure 17. Two dimensional snapshot of gas surface density normalized to its initial profile for the run M1B10 at time  $t = 260$  orbits. We see the accelerated mass redistribution driving mass out of the computational domain.

There is no self-regulated GI in this case and the gas surface density shows high temporal variability. This might be due to the fact that the highly massive disk exert torques of high magnitude, causing very fast redistribution of material in the disk. This is depicted in the 2D surface density snapshot of the M1B10 run in Fig. 17.

### 5.2.3 Mass loss

Figure 18 represents the variation of total mass in terms of the initial mass over time for our models. We see that there was about 6% of the mass lost in the case of M2B10 over 1000 orbits. The mass losses from the computational domain at the onset of gravitational instability introduce net angular momentum losses in the domain, causing an accretion burst onto the central star. We also note that the relative mass appears to be increasing after  $t = 600$  orbits for M3B10 and M5B10, due to small amount of material entering into the computational domain because of boundary effects likely from the damping zone or the outer edge.

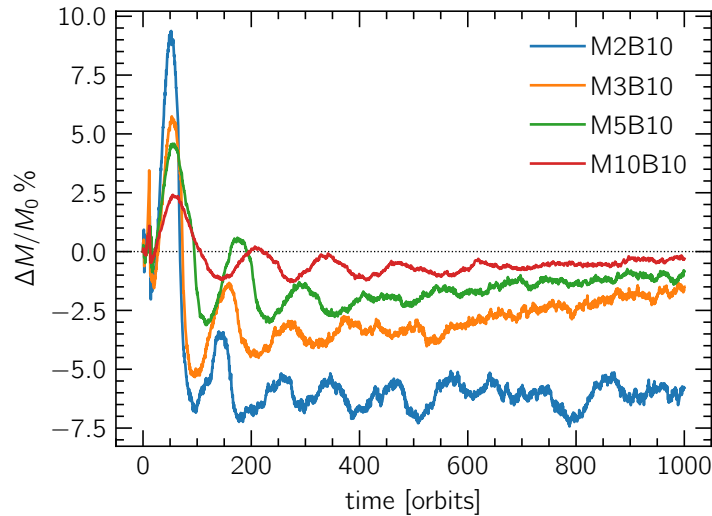


Figure 18. Mass loss (%) from the computational domain in models M2B10, M3B10, M5B10 and M10B10 over time. We see that the most massive disk loses proportionally more mass (6%) compared to the others.

### 5.2.4 Toomre parameter and the disk aspect ratios

Figure 19 (left) shows the density-weighted Toomre parameter for all our models with a constant  $\beta = 10$ . We find a value of  $Q \approx 1$  in all the cases, indicating self-regulation of the disk back to marginal stability. We also plot the disk aspect ratios on the right, with vertical dashed lines indicating those found by [Béthune et al. \(2021\)](#) in their 3D simulations. We see that the values match closely between 2D and 3D with a slight deviation in the run M2B10, but overall it settles into a constant value.

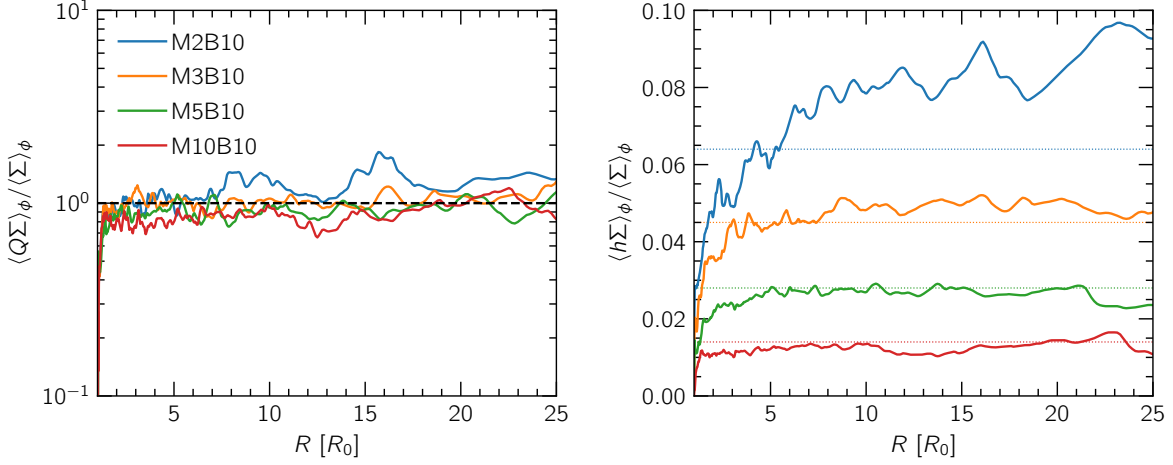


Figure 19. Density-weighted Toomre parameter  $Q$  (left) and aspect ratio  $h$  (right) against the radial distance for models M2B10, M3B10, M5B10 and M10B10. The dashed line on the first plot represents  $Q \approx 1$ .

Model	$M_{\text{disk}}(M_\star)$	$\beta$	$h$	$\alpha$	$\tan(i)$
M2B10	1/2	10	0.064	$0.13 \pm 0.02$	$0.24 \pm 0.006$
M3B10	1/3	10	0.045	$0.117 \pm 0.02$	$0.238 \pm 0.003$
M5B10	1/5	10	0.028	$0.109 \pm 0.06$	$0.232 \pm 0.01$
M10B10	1/10	10	0.014	$0.07 \pm 0.04$	$0.22 \pm 0.03$

Table 2. List of the model parameters with the computed total stresses  $\alpha$  and the pitch angles  $\tan(i)$  with their respective standard deviation errors.

### 5.2.5 Angular momentum transport

We compute stresses as we did previously with the procedure outlined in Sect. 3.6 and plot the total stress ( $\alpha = \alpha_G + \alpha_R$ ) for our models in Fig. 20. In all cases with  $\beta = 10$  we found the value of stress to be close to the expected analytical value of 0.1, but with some error bars. This supports the hypothesis that the orbital energy extracted from the GI turbulence indeed counteracts cooling (Gammie, 2001). The values of  $\alpha$  are listed with their standard deviation error bars in Table 2.

The total stress for the run M5B10 matches  $\alpha_{\text{LTE}}$  the closest, with the least massive disk model M10B10 showing the largest deviation. The gravitational stresses are roughly of the same order of magnitude in all our runs, and the main contribution to the deviation comes from the Reynolds stresses as seen in the right panel of Fig. 20. We attribute this to an under-estimated (a net negative average value) Reynolds stress that we obtain for the latter model. Overall, self-gravity is the most dominant driver of angular momentum transport in the system. We note that the error bars are larger than those in the 3D simulations of Béthune et al. (2021), likely due to the differences in computing the stress and our assumptions of the vertical length scale.

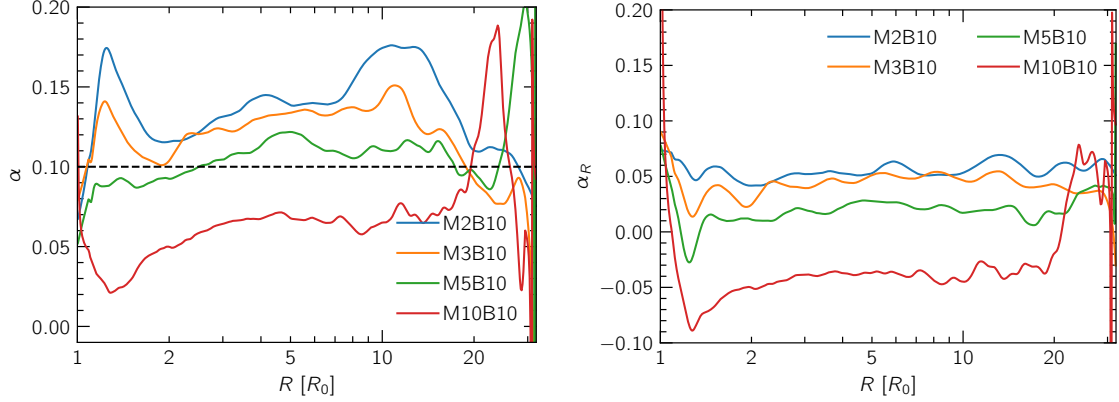


Figure 20. Radial profiles of total normalized stress  $\alpha$  (left) and Reynolds stress  $\alpha_R$  (right) for the runs M2B10, M3B10, M5B10 and M10B10. The dashed line indicates the value  $\alpha_{\text{LTE}} = 0.1$ .

### 5.2.6 Pitch angles and dispersion relations

We follow the same method outlined in Sect. 5.1.6 to obtain the pitch angles of the spirals. The values of  $\tan(i)$  for the different models are listed in Table 2 with their respective error bars. Figure 21 shows the 2D density fluctuations for the highest and lowest disk mass cases in our models, corresponding to the runs M2B10 and M10B10. We see the denser spiral structure with decreasing disk mass. The dashed lines provide an approximate linear fit, with the mean pitch angles corresponding to  $i = 13.5^\circ$  and  $12.4^\circ$  for the two runs respectively.

The calculated radial wavenumber was  $m_0 \approx 3.5 \pm 0.7$  for M2B10,  $m_0 \approx 5.5 \pm 0.5$  for M3B10 and  $m_0 \approx 18.2 \pm 3.4$  for M10B10 and the observed spirals were of the order  $m \approx \{3, 5\}, \{4, 6\}, \{9, 12\}$  for each of the runs respectively. For the lower disk mass cases, the pattern was similar to that of  $m \approx m_0$  but for higher disk mass cases it was much lower. We do identify that there

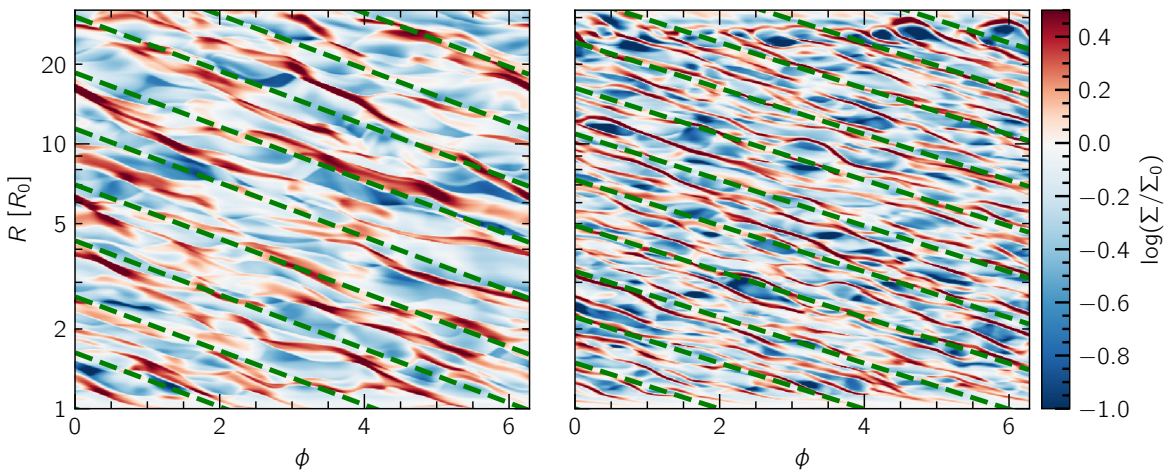


Figure 21. Two-dimensional density fluctuations in the  $R\phi$  plane for the models M2B10 and M10B10 respectively (highest and lowest  $q$ ). The dashed diagonal lines highlight the spirals using a fit based on their mean pitch angle, as previously discussed.

might be significant deviation while identifying spirals with our method compared to a full Fourier analysis.

### 5.3 Comparison to the 3D simulations

In this section, we aim to understand the key differences in results between our 2D simulations and the 3D models by [Béthune et al. \(2021\)](#). While self-gravity is treated with different methods in the two approaches, we use initial conditions, resolution and model parameters close to the 3D paper to understand what inherently changes in our results. However, there are some changes in our implementation, with our outflow outer boundary compared to the reflective one used by [Béthune et al. \(2021\)](#), wave damping on both radial boundaries, and inclusion of the indirect term, which explains the differences in the evolution of the total mass in our computational domain. The high mass disk with  $q = 1$  was rendered very unstable in our simulations, flushing mass out of the domain, whereas the 3D paper showed that they do see spirals of the order  $m = 2$  and occasionally one armed spirals and they saw a 25% decrease in mass over 300 orbits.

The 2D snapshots of the gas surface densities look quite similar to the ones seen in 3D. The disk takes roughly the same number of orbits to fully develop and settle into GI saturation. Disks settle into a marginal stability  $Q \approx 1$ , with the density-weighted Toomre parameter in 3D matching well with the 2D simulations (where both the azimuthally averaged and density weighted  $Q$  approach unity) indicating that the turbulence is dominantly GI driven. We see that the normalized total stresses agree with  $\alpha_{\text{LTE}}$  quite well in both cases, with deviations being more prominent in 2D. The two-dimensional approach to computing these stresses involves summing up surface densities for the Reynolds stress as compared to volume densities, and further requires an assumption for a vertical length scale while estimating the gravitational stresses (see Eq. (25)). That considered, we still found that on average, it matches the 3D result quite close, including the negative average Reynolds stress contribution that [Béthune et al. \(2021\)](#) found for the model M10B10.

The 3D models use an autocorrelation to estimate the mean pitch angles, but the values we find with our linear fits very closely match the pitch angles found in their runs, with angles lying between 12–14° for the most to least massive disks. The error bars could be improved by using a method like autocorrelation but our linear fit still stands pretty robust. With the estimated pitch angles, estimates of the radial wavenumber  $k_0$  from the dispersion relations and the related  $m_0$  match quite closely in both 2D and 3D. However, [Béthune et al. \(2021\)](#) show  $m \approx m_0/2$  which is true only for our models with lower disk mass ( $q = 0.2, 0.1$ ). In other cases, we found  $m \approx m_0$  which is what [Cossins et al. \(2009\)](#) reported. We stress that a full Fourier analysis is needed for a clearer picture.

Overall, our quite significantly faster and computationally efficient 2D models match the results from the 3D paper to an extent.

## 5.4 Resolution study

We ran models with resolution  $N_R \times N_\phi = 1036 \times 1024$ , which is twice our normal resolution, for the cases M5B10 and M10B10. Figure 22 shows the gas surface density fluctuations normalized to the initial profile for the both normal (left) and double (right) resolution runs. We see that although the surface density structures look extremely similar—with spirals that show self-similarity and similar pitch angles—on closer inspection the double resolution shows more spirals. To quantify the effect of resolution better, we plotted the normalized stress curves in both cases. We found that the stress went up in the double resolution runs for both M5B10 and M10B10.

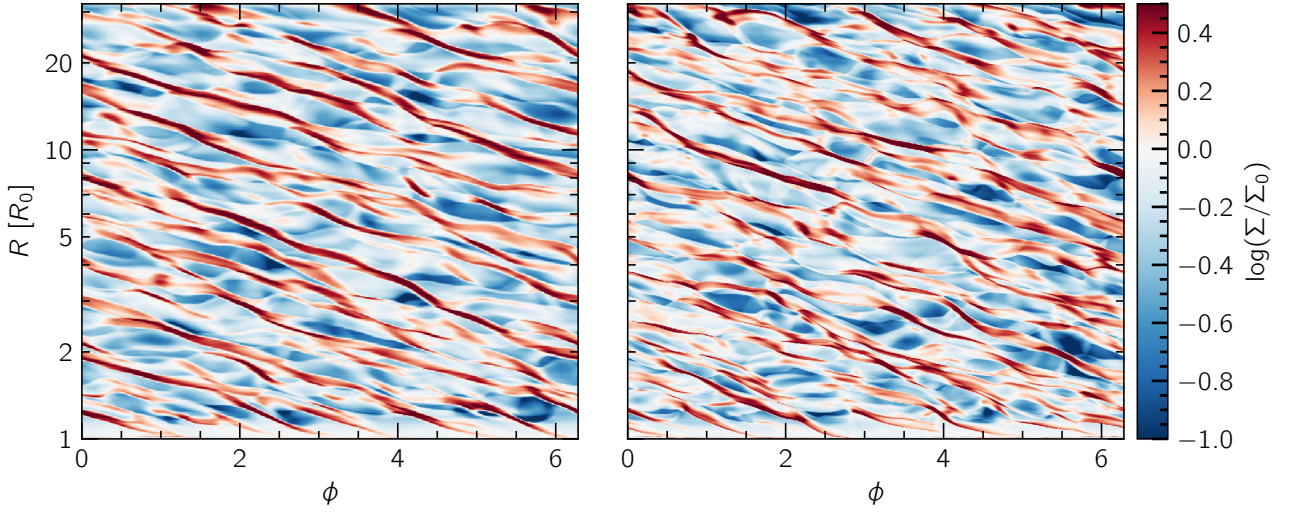


Figure 22. Two-dimensional density fluctuations in the  $R\phi$  plane for the models M5B10 and M5B10D respectively (normal and double resolution). The spiral structure is very similar to each other but we see more features appearing in the double resolution run.

We see that the contribution from Reynolds stress is substantially higher in double resolution runs, indicating that the higher resolution captures other processes, like possible parametric instabilities that cause these velocity fluctuations and the stress to increase ([Riols and Latter, 2018](#)). Parametric instabilities set in after an amplitude threshold where one of the modes of a coupled oscillator becomes unstable and affects the other modes, causing a non-linear instability to develop. This is prominent in fluids, for example, extreme damage is caused to ships that develop these excitations when they bob up and down with frequencies matching the water waves. These features are highly resolution-dependent, as evident in our models, but are not strong enough to perturb the dominant spiral structure forming due to GI saturation. [Béthune et al. \(2021\)](#) do not see parametric instabilities in their normal resolution runs with 3D.

The time-averaged, radially smoothed normalized stress for both models (normal and double resolution) in the case of M5B10 are depicted in Fig. 23. We see that  $\alpha$  goes up to 0.13,

with a large change in  $\alpha_R$  likely due to these parametric excitations. However, for M10B10, we see that the double resolution run matches the analytical  $\alpha_{\text{LTE}}$  with a smaller deviation compared to the otherwise estimated  $\alpha$  (with a negative Reynolds stress contribution) from the normal resolution run. The value corresponds to  $0.13 \pm 0.028$  for M5B10D and  $0.109 \pm 0.0432$  for M10B10D. The pitch angles were identical in both normal and double resolution for both M5B10 and M10B10, with a value of  $i = 12.4^\circ$  for the case of M10B10D.

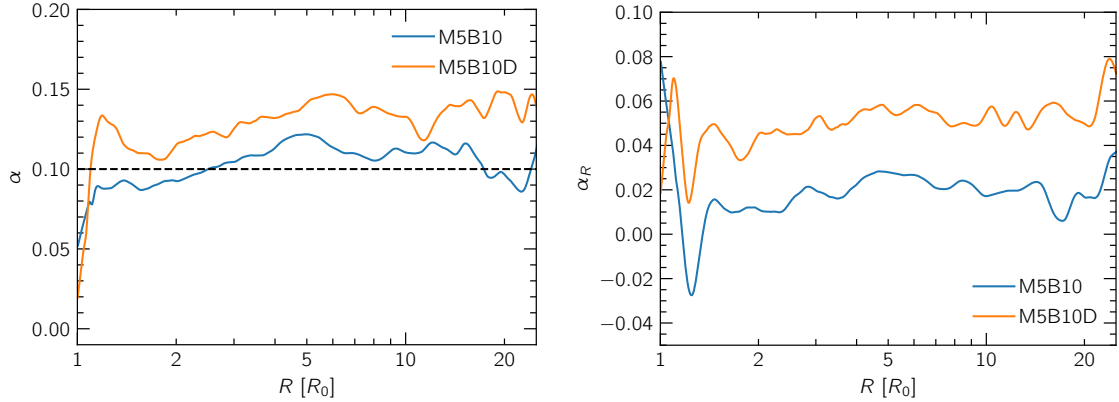


Figure 23. Radial profiles of total normalized stress  $\alpha$  (left) and Reynolds stress  $\alpha_R$  (right) for both M5B10 and M5B10D models. The dashed line indicates the calculated  $\alpha_{\text{LTE}} = 0.1$ .

## 5.5 A note about disk fragmentation

When GI saturation fails to prevent the growth of non-linear perturbations, the unstable disk breaks up into clumps, or fragments. Fragmentation is considered an important process in the context of protoplanetary disks, as it can lead to masses that can act as planet precursors. Disk fragmentation occurs as a result of fast cooling in disks. When the cooling is rapid, the orbital energy extracted due to the GI is insufficient to heat the disk against the cooling and the disk breaks up into fragments. Fragmentation can also be driven by accretion, due to infall of material from the external environment causing the material to clump.

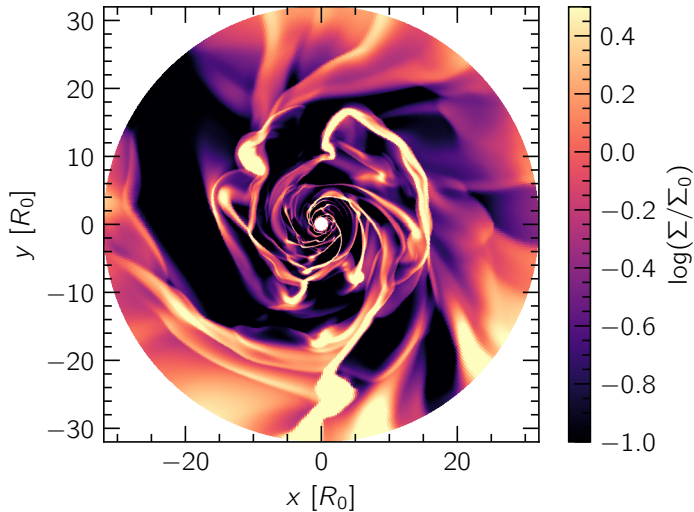


Figure 24. Two-dimensional gas surface density snapshot normalized to its initial profile for the model M2B1 ( $q = 0.5$  and  $\beta = 1$ ) after 200 orbits. We can clearly see that the disk fragments into clumps at various radii in the disk.

The fragmentation boundary, that is, the critical value of  $\beta$  required for the disk to clump has been largely studied with numerical simulations. The value is estimated to be somewhere close to  $\beta_{\text{crit}} \approx 10$ . Two-dimensional simulations where the gravitational force was smoothed on the scale height  $H$  of the disk have previously demonstrated fragmentation at much lower values of  $\beta \lesssim 3$  (Paardekooper et al., 2011).

We chose a value of  $\beta = 1$  to test the results of our model and found that the disk fragments at a very early stage of 200 orbits. Figure 24 shows a 2D gas surface density snapshot of our model M2B10 with clearly visible clumps of material at different radii in the disk. Figure 25 shows the radial variation of azimuthally averaged gas surface density against its initial profile. The location of the peaks in the gas surface density are marked with dotted lines and we see fragments at  $11.5$ ,  $16$  and  $24 R_0$ . This is in good agreement with the simulations done by Moldenhauer (2018). They also saw fragmentation in disks with  $\beta > 1$ , but either they take much longer to develop, or they are resolved in much higher resolutions in compar-

ison to smaller smoothing lengths. The caveats behind the differences in the fragmentation boundary between 2D and 3D simulations lies in the assumptions behind the 2D treatment of self-gravity.

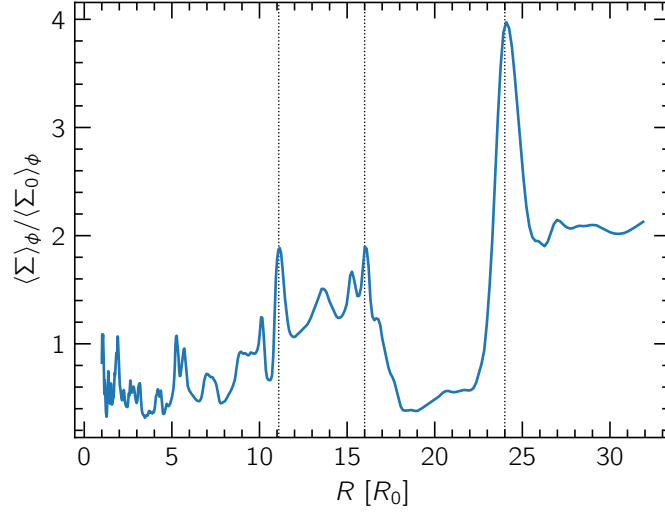


Figure 25. Azimuthally averaged gas surface density profile normalized to its initial profile for model M2B1. The density bumps can be easily identified in the plot. The vertical dotted lines correspond to the radii at which these fragments are located.



## 6 Discussion and conclusions

In this project, we performed 2D global hydrodynamics simulations of gaseous, inviscid, non-magnetized self-gravitating disks with different star–disk mass ratios. We employ an ideal gas equation of state and treat cooling with a parametrized prescription in the disk. These disks, as previously discussed, either fragment under fast cooling conditions or settle into a quasi-steady marginally stable state. While the former question has been previously addressed by 2D simulations, we attempted to look at the latter scenario. The spiral arm morphology and amplitudes have been studied globally with grid and SPH simulations before, and we compared our results to them. We list our main findings below:

1. We found that our results agree with the theory in [Gammie \(2001\)](#), where self-gravitating disks in the marginally stable  $Q \approx 1$  regime are modeled locally. Angular momentum transport is governed by gravitational stress, the value of which is in the same order as viscous  $\alpha$  disks in thermal equilibrium.
2. Our 2D models are fast, computationally efficient and the results reproduce the findings in the 3D paper quite well. We note that there are caveats while treating quantities like turbulent stress in 2D and the deviations are likely caused by the method.
3. Spirals in the disk do not shear, show self-similarity and form at pitch angles constant in radius and time. This self-similarity is expected from our model setup (constant  $\beta, h$ ). The spirals are restricted to a short range of wavenumbers estimated using the dispersion relations. We found that for higher disk–star mass ratios, the wavenumbers were of the order predicted by the 2D linear disk theory, but for lower values we found fewer spirals than the predicted number.
4. We found that the values of the total stress go up with increasing resolution. The likely cause might be that a higher resolution resolves other instabilities, like parametric excitations that could contribute to the velocity fluctuations affecting the average values of the stress.
5. We find evidence for disk fragmentation in our models under fast cooling with a  $\beta = 1$ , previously confirmed in the simulations by [Moldenhauer \(2018\)](#). Disk fragmentation is in itself a vast topic of interest, and depends on the thermodynamics of the system.

Our simulations, although they cover a good set of parameter space, are not fully indicative of all effects that could alter spiral morphology. Different treatments of the vertical structure, gas thermodynamics, treatment of stellar radiation, tidal effects—could alter global wave modes in the disk and are subjects of past and ongoing research. Moreover, two-dimensional simulations do not address vertical flows that could be caused by GI turbulence.

With great amounts of progress in observations of protoplanetary disks in recent times, we are at the onset of being able to study the morphology and structure of the material in the disk, either by imaging or line emissions. Spiral structures have been detected in disks, with

scattered light images in the NIR, molecular lines and dust emission. Whether or not these are GI driven is a question that can be answered by estimating disk masses and temperatures more accurately. With milliarcsecond resolutions in the sub-millimeter bands, we might even be able to differentiate these spiral substructures and carry out improved models that study them.

## 7 Acknowledgments

I am grateful for the computational resources provided by the Computational Physics Ti<sub>c</sub><sup>1/2</sup>bingen (CPT) and the Baden-Württemberg High Performance Computing cluster BinAC, which I used to run all of my simulations.

I take this opportunity to reflect and express my gratitude to everyone that helped me get to this point in my career. I would like to thank my late advisor, and teacher, Willy Kley with whom I got to learn from and work with for one and a half years, for his guidance and encouragement. His scientific legacy as a researcher and mentor continues to be a source of inspiration. I am indebted to the opportunities I got from him as a graduate student, from learning how to run a simulation, to writing a research paper, presenting it in conferences and securing a PhD position.

I would like to thank Christoph, for always welcoming me with a smile to address my doubts about everything under the sun—exercise sheets, exams, PhD applications, credit points, funding and thesis deadlines. I thank Will for guiding me throughout my master thesis and helping me every time I was stuck. His advice has been key in not only improving my work but also how I work. I thank Tobi for helping me with the self-gravity module and Alex, who spent hours trying to get me to understand where and why my code failed, and taught me how to fix it. I probably learned more about numerics and hydrodynamics from spending the better part of the last year working with Anna and Alex, than I ever did before. I thank all my professors, and everyone at CPT for their lovely company, especially my office mates Jibin, Anna and Katyayani. I thank all my friends here and back in India, for being such a strong support system.

Most of all, I would like to thank my family—my boyfriend, my mum and dad without whom this whole endeavor would have been moot. Thanks for believing in me.



## References

- ALMA Partnership, Brogan, C. L., Pérez, L. M., Hunter, T. R., Dent, W. R. F., Hales, A. S., Hills, R. E., Corder, S., Fomalont, E. B., Vlahakis, C., Asaki, Y., Barkats, D., Hirota, A., Hodge, J. A., Impellizzeri, C. M. V., Kneissl, R., Liuzzo, E., Lucas, R., Marcelino, N., Matsushita, S., Nakanishi, K., Phillips, N., Richards, A. M. S., Toledo, I., Aladro, R., Broguiere, D., Cortes, J. R., Cortes, P. C., Espada, D., Galarza, F., Garcia-Appadoo, D., Guzman-Ramirez, L., Humphreys, E. M., Jung, T., Kamenó, S., Laing, R. A., Leon, S., Marconi, G., Mignano, A., Nikolic, B., Nyman, L. A., Radiszcz, M., Remijan, A., Rodón, J. A., Sawada, T., Takahashi, S., Tilanus, R. P. J., Vila Vilaro, B., Watson, L. C., Wiklind, T., Akiyama, E., Chapillon, E., de Gregorio-Monsalvo, I., Di Francesco, J., Gueth, F., Kawamura, A., Lee, C. F., Nguyen Luong, Q., Mangum, J., Pietu, V., Sanhueza, P., Saigo, K., Takakuwa, S., Ubach, C., van Kempen, T., Wootten, A., Castro-Carrizo, A., Francke, H., Gallardo, J., Garcia, J., Gonzalez, S., Hill, T., Kaminski, T., Kurono, Y., Liu, H. Y., Lopez, C., Morales, F., Plarre, K., Schieven, G., Testi, L., Videla, L., Villard, E., Andreani, P., Hibbard, J. E., and Tatematsu, K. (2015). The 2014 ALMA Long Baseline Campaign: First Results from High Angular Resolution Observations toward the HL Tau Region. *ApJ*, 808(1):L3.
- Balbus, S. A. and Papaloizou, J. C. B. (1999). On the Dynamical Foundations of  $\alpha$  Disks. *ApJ*, 521(2):650–658.
- Baruteau, C. (2008). *Toward predictive scenarios of planetary migration*. PhD thesis.
- Benisty, M., Juhasz, A., Boccaletti, A., Avenhaus, H., Milli, J., Thalmann, C., Dominik, C., Pinilla, P., Buenzli, E., Pohl, A., Beuzit, J. L., Birnstiel, T., de Boer, J., Bonnefoy, M., Chauvin, G., Christiaens, V., Garufi, A., Grady, C., Henning, T., Huelamo, N., Isella, A., Langlois, M., Menard, F., Mouillet, D., Olofsson, J., Pantin, E., Pinte, C., and Pueyo, L. (2015). VizieR Online Data Catalog: Polarized images of MWC758 (Benisty+, 2015). *VizieR Online Data Catalog*, pages J/A+A/578/L6.
- Bertin, G. (1997). Self-regulated Accretion Disks. *ApJ*, 478(2):L71–L74.
- Bertin, G. (2014). *Dynamics of Galaxies*.
- Bertin, G. and Lodato, G. (1999). A class of self-gravitating accretion disks. *A&A*, 350:694–704.
- Béthune, W., Latter, H., and Kley, W. (2021). Spiral structures in gravito-turbulent gaseous disks. *A&A*, 650:A49.
- Binney, J. and Tremaine, S. (1987). *Galactic dynamics*.
- Binney, J. and Tremaine, S. (2011). *Galactic dynamics*, volume 13. Princeton university press.
- Boley, A. C., Mejía, A. C., Durisen, R. H., Cai, K., Pickett, M. K., and D’Alessio, P. (2006). The Thermal Regulation of Gravitational Instabilities in Protoplanetary Disks. III. Simulations with Radiative Cooling and Realistic Opacities. *ApJ*, 651(1):517–534.

- Cameron, A. G. W. (1978). Physics of the primitive solar accretion disk. *Moon and the planets*, 18(1):5.
- Cossins, P., Lodato, G., and Clarke, C. J. (2009). Characterizing the gravitational instability in cooling accretion discs. *MNRAS*, 393(4):1157–1173.
- de Val-Borro, M., Edgar, R. G., Artynowicz, P., Ciecielag, P., Cresswell, P., D’Angelo, G., Delgado-Donate, E. J., Dirksen, G., Fromang, S., Gawryszczak, A., Klahr, H., Kley, W., Lyra, W., Masset, F., Mellema, G., Nelson, R. P., Paardekooper, S. J., Peplinski, A., Pierens, A., Plewa, T., Rice, K., Schäfer, C., and Speith, R. (2006). A comparative study of disc-planet interaction. *MNRAS*, 370(2):529–558.
- Desai, K. M., Steiman-Cameron, T. Y., Michael, S., Cai, K., and Durisen, R. H. (2019). A 3D hydrodynamics study of gravitational instabilities in a young circumbinary disc. *MNRAS*, 483(2):2347–2361.
- Gammie, C. F. (2001). Nonlinear Outcome of Gravitational Instability in Cooling, Gaseous Disks. *ApJ*, 553(1):174–183.
- Garufi, A., Quanz, S. P., Avenhaus, H., Buenzli, E., Dominik, C., Meru, F., Meyer, M. R., Pinilla, P., Schmid, H. M., and Wolf, S. (2013). Small vs. large dust grains in transitional disks: do different cavity sizes indicate a planet?. SAO 206462 (HD 135344B) in polarized light with VLT/NACO. *A&A*, 560:A105.
- Harten, A. (1983). High resolution schemes for hyperbolic conservation laws. *Journal of Computational Physics*, 49(3):357–393.
- Kratter, K. and Lodato, G. (2016). Gravitational Instabilities in Circumstellar Disks. *ARA&A*, 54:271–311.
- Kuiper, G. P. (1951). On the origin of the solar system. *Proceedings of the National Academy of Sciences*, 37(1):1–14.
- Lodato, G. (2007). Self-gravitating accretion discs. *Nuovo Cimento Rivista Serie*, 30:293.
- Lodato, G. and Rice, W. K. M. (2004). Testing the locality of transport in self-gravitating accretion discs. *MNRAS*, 351(2):630–642.
- Lodato, G. and Rice, W. K. M. (2005). Testing the locality of transport in self-gravitating accretion discs - II. The massive disc case. *MNRAS*, 358(4):1489–1500.
- Lynden-Bell, D. and Kalnajs, A. J. (1972). On the generating mechanism of spiral structure. *MNRAS*, 157:1.
- Mann, R. K., Andrews, S. M., Eisner, J. A., Williams, J. P., Meyer, M. R., Di Francesco, J., Carpenter, J. M., and Johnstone, D. (2015). Protoplanetary Disk Masses in the Young NGC 2024 Cluster. *ApJ*, 802(2):77.

- Meru, F. and Bate, M. R. (2011a). Non-convergence of the critical cooling time-scale for fragmentation of self-gravitating discs. *MNRAS*, 411(1):L1–L5.
- Meru, F. and Bate, M. R. (2011b). On the fragmentation criteria of self-gravitating protoplanetary discs. *MNRAS*, 410(1):559–572.
- Mestel, L. (1963). On the galactic law of rotation. *MNRAS*, 126:553.
- Michael, S. and Durisen, R. H. (2010). Stellar Motion Induced by Gravitational Instabilities in Protoplanetary Disks. *arXiv e-prints*, page arXiv:1005.3744.
- Mignone, A., Bodo, G., Massaglia, S., Matsakos, T., Tesileanu, O., Zanni, C., and Ferrari, A. (2007). PLUTO: a Numerical Code for Computational Astrophysics. In *JENAM-2007, “Our Non-Stable Universe”*, pages 96–96.
- Moldenhauer, T. (2016). Simulating two-dimensional self-gravitating disks on GPUs.
- Moldenhauer, T. (2018). Treating self-gravity in two-dimensional simulations of protoplanetary disks.
- Müller, T. W. A., Kley, W., and Meru, F. (2012). Treating gravity in thin-disk simulations. *A&A*, 541:A123.
- Muto, T., Grady, C. A., Hashimoto, J., Fukagawa, M., Hornbeck, J. B., Sitko, M., Russell, R., Werren, C., Curé, M., Currie, T., Ohashi, N., Okamoto, Y., Momose, M., Honda, M., Inutsuka, S., Takeuchi, T., Dong, R., Abe, L., Brandner, W., Brandt, T., Carson, J., Egner, S., Feldt, M., Fukue, T., Goto, M., Guyon, O., Hayano, Y., Hayashi, M., Hayashi, S., Henning, T., Hodapp, K. W., Ishii, M., Iye, M., Janson, M., Kandori, R., Knapp, G. R., Kudo, T., Kusakabe, N., Kuzuhara, M., Matsuo, T., Mayama, S., McElwain, M. W., Miyama, S., Morino, J. I., Moro-Martin, A., Nishimura, T., Pyo, T. S., Serabyn, E., Suto, H., Suzuki, R., Takami, M., Takato, N., Terada, H., Thalmann, C., Tomono, D., Turner, E. L., Watanabe, M., Wisniewski, J. P., Yamada, T., Takami, H., Usuda, T., and Tamura, M. (2012). Discovery of Small-scale Spiral Structures in the Disk of SAO 206462 (HD 135344B): Implications for the Physical State of the Disk from Spiral Density Wave Theory. *ApJ*, 748(2):L22.
- Nayakshin, S., Cuadra, J., and Springel, V. (2007). Simulations of star formation in a gaseous disc around Sgr A\* - a failed active galactic nucleus. *MNRAS*, 379(1):21–33.
- Ogilvie, G. I. and Lubow, S. H. (2002). On the wake generated by a planet in a disc. *MNRAS*, 330(4):950–954.
- Paardekooper, S.-J., Baruteau, C., and Meru, F. (2011). Numerical convergence in self-gravitating disc simulations: initial conditions and edge effects. *MNRAS*, 416(1):L65–L69.
- Rice, W. K. M., Lodato, G., and Armitage, P. J. (2005). Investigating fragmentation conditions in self-gravitating accretion discs. *MNRAS*, 364(1):L56–L60.

- Riols, A. and Latter, H. (2018). Spiral density waves and vertical circulation in protoplanetary discs. *MNRAS*, 476(4):5115–5126.
- Shakura, N. I. and Sunyaev, R. A. (1973). Black holes in binary systems. Observational appearance. *A&A*, 24:337–355.
- Shepherd, D. S., Borders, T., Claussen, M., Shirley, Y., and Kurtz, S. (2004). The Circumstellar Environment of the Early B Protostar G192.16-3.84 and the Discovery of a Low-Mass, Protostellar Core. *ApJ*, 614(1):211–220.
- Shepherd, D. S., Claussen, M. J., and Kurtz, S. E. (2001). Evidence for a Solar System-Size Accretion Disk Around the Massive Protostar G192.16-3.82. *Science*, 292(5521):1513–1518.
- Shi, J.-M. and Chiang, E. (2014). Gravito-turbulent Disks in Three Dimensions: Turbulent Velocities versus Depth. *ApJ*, 789(1):34.
- Spitzer, Lyman, J. (1942). The Dynamics of the Interstellar Medium. III. Galactic Distribution. *ApJ*, 95:329.
- Steiman-Cameron, T. Y., Durisen, R. H., Boley, A. C., Michael, S., and McConnell, C. R. (2013). Convergence Studies of Mass Transport in Disks with Gravitational Instabilities. II. The Radiative Cooling Case. *ApJ*, 768(2):192.
- Sudarshan, P., Penzlin, A. B. T., Ziampras, A., Kley, W., and Nelson, R. P. (2022). How cooling influences circumbinary discs. *A&A*, 664:A157.
- Thun, D. and Kley, W. (2018). Migration of planets in circumbinary discs. *A&A*, 616:A47.
- Toomre, A. (1964). On the gravitational stability of a disk of stars. *ApJ*, 139:1217–1238.
- Toro, E. F., Spruce, M., and Speares, W. (1994). Restoration of the contact surface in the HLL-Riemann solver. *Shock Waves*, 4(1):25–34.
- Van Leer, B. (1974). Towards the ultimate conservative difference scheme. II. Monotonicity and conservation combined in a second-order scheme. *Journal of computational physics*, 14(4):361–370.
- Wagner, K., Apai, D., Kasper, M., and Roberto, M. (2015). Discovery of a Two-armed Spiral Structure in the Gapped Disk around Herbig Ae Star HD 100453. *ApJ*, 813(1):L2.
- Young, M. D. and Clarke, C. J. (2015). Dependence of fragmentation in self-gravitating accretion discs on small-scale structure. *MNRAS*, 451(4):3987–3994.

